easyMRFM: increasing sample accessibility for SQUID-detected Magnetic Resonance Force Microscopy

Stolte, Evert

Citation

Stolte, E. (2021). *easyMRFM: increasing sample accessibility for SQUID-detected Magnetic Resonance Force Microscopy.*

easyMRFM: increasing sample accessibility for SQUID-detected Magnetic Resonance Force Microscopy

THESIS

submitted in partial fulfillment of the
requirements for the degree of

MASTER OF SCIENCE
in
PHYSICS

Author :	Evert Stolte
Student ID :	1671871
Supervisor :	Tjerk Oosterkamp
2nd corrector :	Martina Huber

Leiden, The Netherlands, August 30, 2021

easyMRFM: increasing sample accessibility for SQUID-detected Magnetic Resonance Force Microscopy

Evert Stolte

Huygens-Kamerlingh Onnes Laboratory, Leiden University
P.O. Box 9500, 2300 RA Leiden, The Netherlands

August 30, 2021

Abstract

Magnetic Resonance Force Microscopy (MRFM) is a sensitive method to investigate spin systems, which uses a flexible cantilever as mechanical amplifier of the forces on its magnetic tip. However, MRFM is generally limited in its application at milliKelvin temperatures because existing devices rely on laser interferometry to detect cantilever deflection, which heats the cantilever, leaving many condensed matter systems out of reach for MRFM. Furthermore, lower temperatures correspond to lower cantilever force noise, so samples with more diluted spins could be investigated. SQUID-detected MRFM, using the flux induced by a moving cantilever tip, does allow for operation at milliKelvin temperatures. Yet, SQUID-detecting setups have still been limited in sample accessibility because the detection loop is printed on the sample. This thesis reports on the construction of a SQUID-detected MRFM device that employs a single probe head design to overcome the issue. The design choices and assembly methods for this device, called the easyMRFM, are discussed, as well as models to predict the sensitivity. It was found that the coupling is large enough to do optimisations in liquid helium dipstick experiments, although the thermal cantilever motion signal will only barely rise above the flux noise level. Lastly, a room-temperature magnetometry setup for cantilever chips is discussed that has proven useful in characterising cantilevers before mounting them in more permanent setups.

Contents

1 **Introduction** **1**
  1.1 Magnetic Resonance Force Microscopy for condensed matter physics 1
  1.2 A cantilever in a magnetic field 4

2 **Device Design** **9**
  2.1 Cantilever chip 10
  2.2 Pick-up loop chip 12
  2.3 SQUID chip 15
  2.4 Wire bonds 17
  2.5 Piezo element 20
  2.6 Copper mounting structure and titanium flexture hinge micro-positioning 20
  2.7 Sample stage 23
  2.8 Assembly 23

3 **Models for the cantilever deflection signal** **31**
  3.1 Coupling between the cantilever and pick-up loop 31
  3.2 Coupling between pick-up loop and SQUID 34
  3.3 Coupling to SQUID with a transformer 36
  3.4 Coupling to SQUID with aluminium wire bonds 37
  3.5 Measuring thermal cantilever motion 39

4 **Characterising cantilevers at room temperature** **41**
  4.1 Fringe visibility in the optical detection of cantilever deflection 42
  4.2 Measuring the frequency shift in a homogeneous magnetic field 45

4.3 Driving the cantilever magnetically 47
4.4 Detection of the thermal motion of the cantilever 49

5 Future steps towards magnetic resonance experiments 51
5.1 B_0-field with Plugge coil 51
5.2 Options for the B_1-field 55

6 Conclusions 57

7 Acknowledgements 59

Version of August 30, 2021– Created August 30, 2021 - 14:44

Chapter 1

Introduction

1.1 Magnetic Resonance Force Microscopy for condensed matter physics

The spins of electrons in solid-state materials are directly involved in many phenomena in condensed matter physics, from bulk (ferro-) magnetism, to nanometer-scale spin waves[1] and the atomic-scale Kondo-effect[2]. Probing spins and their local magnetic environment is a natural way to investigate these phenomena. In other condensed matter systems, the presence of spins can interfere with the system instead. Particularly in solid state qubits, the coupling to other 2-level systems like free electrons spins results in undesired decoherence of the qubit, which is itself a two-level system. In this case, the probing of spin properties can further the understanding of decoherence sources and lead to improved production methods to avoid these sources in the future.

A good example to illustrate the relevance of research into this mechanism of decoherence is superconducting qubits that utilise Al-Al_2O_3-Al Josephson junctions. Although considerable effort has been put into avoiding the formation of free spins in proximity of the junctions during the production process, the observed decoherence times of the resulting devices suggest a sizeble amount of 2-level systems is still present. A proposed hypothesis points to the spins from single unbounded orbital electrons right at the boundary between Aluminium and Aluminium Oxide as the origin of these impurities. These so-called 'dangling bonds' only form between the layers as they are fabricated on top of one another and would thus be inaccessible to surface probing techniques both before and after a production step.

In order to confirm this hypothesis, the right spin-probing technique needs to be employed. Various methods exist for probing the properties of electron spins at different length scales: Electron Spin Resonance (ESR) spectroscopy [3], spin-polarised STM[4], ESR-STM[5], and NV magnetometry[6]. However, it is Magnetic Resonance Force Microscopy (MRFM)[7][8] that is most suitable to investigate Al-Al_2O_3-Al junctions.

MRFM employs magnetic resonance, as do many other spin-probing methods. Spins are polarised with one magnetic field B_0 and magnetically driven at the Larmor (angular) frequency ω_L to precess with another field B_1.

$$\hbar\omega_L = g_e \mu_B B_0 \tag{1.1}$$

where μ_B is the Bohr magneton, a physical constant, and g_e is the Landé g-factor, $g_e = 2.0023$ for the free electron. A local field alters the effective magnetic field strength and thus the Larmor frequency is also dependent on the environment of electrons. Furthermore, the relatively slow and likewise environment-dependent decay to the equilibrium spin-orientations can be studied to infer material properties[3].

MRFM sets itself apart in the method of probing the magnetic response. The deflection of a magnetically-coupled flexible cantilever is used as a force probe for the magnetic field generated by electron spins in a sample, and thus their decay in magnetic resonance experiments. Using magnetic resonance with a B_0 field with a gradient allows for detection of spin properties under the surface at a controlled depth, because only those spins in the resonant slice with the corresponding Larmor frequency precess as they decay to an unpolarised state. The addition of the cantilever as probe localises the measurement and allows for microscopy.

Different variants of MRFM exist. The magnetic coupling between the spins in the sample and the cantilever can be achieved by attaching a magnetic particle at the tip of the cantilever (magnet-on-tip), or conversely mounting the sample on the cantilever tip and oscillating above a nanomagnet (sample-on-tip). In practice, a high local field gradient needed for a thin resonance slice is provided by the nanomagnet itself. Higher gradients can be achieved with the surface-attached magnets of the sample-on-tip geometry, which makes this more suitable for imaging. However, the generality of the possible samples is reduced. The magnet-on-tip allows for more flexibility in sample preparation.

Furthermore, there is variation in the method of extracting the deflection of the cantilever. MRFM is fundamentally limited by the achievable force sensitivity, so reducing the thermal force noise is a critical part of an

MRFM setup. For a mechanical cantilever at the resonant frequency, the thermal force noise can be derived by equipartition and is given by [9]

$$\sqrt{S_F} = \sqrt{4k_bT\frac{k}{\omega_0 Q} \cdot BW} \tag{1.2}$$

where k is the stiffness of the cantilever, $\omega_0 = 2\pi f_0$ is the resonant frequency, Q is the quality factor, and BW is the measurement bandwidth.

A traditional method of measuring the deflection is to use laser interferometry, with the beam focused on the cantilever tip. Laser-MRFM has been effective as a non-invasive technique in, for example, biological samples with 3-dimensional spatial resolutions as high as 5 nm[10]. The disadvantage of this scheme is the heating of the cantilever from the laser, because a higher temperature increases the force noise. A benefit of studying condensed matter systems is the ability, and sometimes necessity, of utilising extremely low milliKelvin temperatures. A scheme that can measure the cantilever displacement at these temperatures, can take advantage of an extremely low thermal force noise.

Our group has recently developed a SQUID-detected MRFM device capable of measuring diluted electron spin ensembles in diamond[11] and nuclear spins in copper with a detection volume of (40 nm)^3[12]. In this device, operating around 10 mK, the deflection of the cantilever is detected inductively instead of optically. A magnet-on-tip approach was used and a pick-up loop is installed in proximity to the cantilever tip. As the cantilever deflects, the pick-up loop experiences a changing magnetic flux. This flux can then be very accurately measured by a SQUID (superconducting quantum interference device). In a flux-based setup like this, the pick-up loop needs to be in close proximity to the magnetic cantilever tip to get a large enough flux coupling. To do this, it was chosen to fabricate the superconducting loop on the sample itself using lithography and have the SQUID mounted next to the loop on the sample as well.

The limitation of this setup is its versatility as a general probe. The method to fabricate a pick-up loop on a sample surface does not suit all samples. More importantly, it takes a lot of dedicated time, effort and experience to print the loop and SQUID on any sample. In the example of dangling bonds in superconducting qubits, MRFM would be used as a diagnostics tool to determine which step in the many-staged fabrication process is responsible for introducing paramagnetic impurities. This would require a loop to be printed for each sample from every fabrication step, meanwhile risking the introduction of more impurities by the printing process. The impracticality and time consumption of the loop-on-sample

Version of August 30, 2021– Created August 30, 2021 - 14:44

design hampers the broader application of SQUID-detected MRFM.

The solution presented in this thesis makes SQUID-detected MRFM accessible for a wide range of condensed matter applications with a device that has the pick-up loop and SQUID attached next to the cantilever, as a single probe head. This is made possible by the use of mechanical flexure hinges that are used align the loop to the cantilever on micrometer proximity to optimise flux coupling. In this thesis, both the design and assembly of the device, named the 'easyMRFM', will be discussed in chapter 2. Chapter 3 contains an investigation of the capabilities of the easyMRFM using analytical models. Furthermore, chapter 4 explores a method to characterise cantilevers at room temperature in an optical setup before they are mounted in a permanent setup. Chapter 5 outlines the work that still needs to be done before the easyMRFM can be used in experiments on Al-Al_2O_3-Al junctions and in condensed matter physics more generally. The following section will first discuss the mechanics of a cantilever with a magnetic tip in a magnetic field.

1.2 A cantilever in a magnetic field

The magnetisation of the nanomagnet dipoles attached to the tip of the cantilevers is generally in the same direction as the long side of the cantilever, which we define as the z-direction (also the direction of sample approach). A schematic of the different elements relevant for the kinematics can be found in Fig 1.1. Besides being long, the cantilever is also flat (thin in one direction, and thick in the other), so it practically only has a flexible mode in one direction. This direction of cantilever deflection will be labelled the x-direction. In a magnetic resonance experiment, the spins in a sample will be polarised in the z-direction by an external field, parallel with the cantilever. In practice there will always be a slight discrepancy in alignment and the spins should be treated as magnetic dipole moments. In this elementary derivation however, the effective field on the cantilever tip will be approximated by a uniform field $\vec{B}$ with a misalignment. The angle between the cantilever rest position with zero field (= z-direction) and the magnetic field in the x,z-plane will be called θ_0.

As with a simple pendulum, the reality of the deflection is that the mode of movement of the complete cantilever is not a shift in the x-direction, but a rotation of an angle θ around the point of attachment of the cantilever. The rest position of the cantilever without a magnetic field would then correspond to $\theta = 0$. However, it is still only the x-direction movement of the tip of the cantilever that is detected. For the simple pendulum

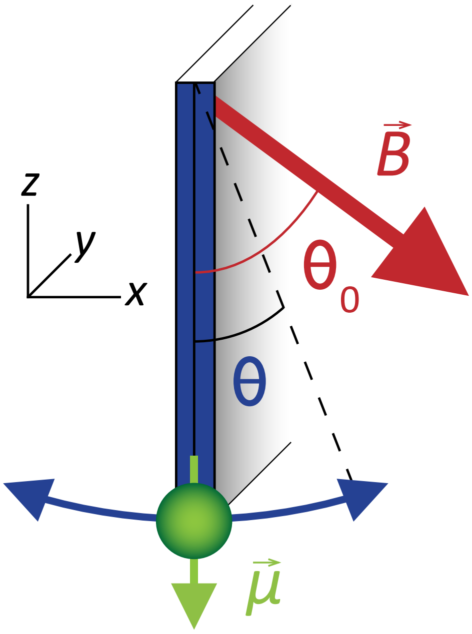

Figure 1.1: *Schematic of MRFM cantilever in a constant magnetic field. The cantilever has a nanomagnet attached at the tip with a magnetic dipole $\vec{\mu}$ polarised in the z-direction. The cantilever can deflect in the x-direction, making an angle θ with the z-axis. The magnetic field is intended to be pointing in the z-direction as well, but might be misaligned by an angle θ_0.*

the transformation from θ to x amounts to elementary trigonometry using $x = l \cdot sin(\theta)$, with l the length of the pendulum, but for the cantilever it needs to be taken into account that it bends when deflected by a force on the tip. This bending effectively reduces the length of the cantilever from the point of view of the tip and can be taken care of by including a geometric factor α in the transformation between θ and x.

$$x = \frac{l}{\alpha} sin(\theta) \approx \frac{l}{\alpha} \cdot \theta \quad \text{when deflection is small} \tag{1.3}$$

The cantilever experiences a restoring force in the x-direction towards the zero-field equilibrium position due to its stiffness k, which can be modelled as a force in an harmonic oscillator.

$$F_k = -kx \tag{1.4}$$

The magnetic field $\vec{B}$ has an interaction with the magnetic dipole moment $\vec{\mu}$ of the magnet at the tip of the cantilever. This results in a torque $\vec{\tau} = \vec{\mu} \times \vec{B}$ on the nanomagnet dipole and, by extent, on the cantilever. As we are mostly interested in what happens in the direction of deflection, the x-component of the force, F_B, on the cantilever tip from the torque can be taken. Again, the bending of the cantilever should be taken into account with the α factor to correct the cantilever length and the angle between the field and the cantilever at any point is $\theta_0 - \theta$.

$$F_B = +|\mu| \cdot |B| \frac{\alpha}{l} \cdot sin(\theta_0 - \theta) \tag{1.5}$$

$$\approx |\mu| \cdot |B| \frac{\alpha}{l} sin(\theta_0) - |\mu| \cdot |B| cos(\theta_0) \cdot (\frac{\alpha}{l}\theta) \tag{1.6}$$

$$= |\mu| \cdot |B| \frac{\alpha}{l} sin(\theta_0) - |\mu| \cdot |B| \left(\frac{\alpha}{l}\right)^2 cos(\theta_0) \cdot x \tag{1.7}$$

Where in the second step the deflection angle is again assumed to be small so the Taylor expansion $sin(\theta_0 - \theta) \approx sin(\theta_0) - \theta \cdot cos(\theta_0)$ and in the third step x is substituted in from Eq 1.3.

The total force on a cantilever in a magnetic field combines Eq (1.4) and Eq (1.7).

$$F_B + F_k = -\left(k + |\mu| \cdot |B| \left(\frac{\alpha}{l}\right)^2 cos(\theta_0)\right) \cdot x + |\mu| \cdot |B| \frac{\alpha}{l} sin(\theta_0) \tag{1.8}$$

This can be interpreted as the magnetic field introducing an offset for the resting position with the constant force in the second term and altering the stiffness in the harmonic first term. An aligned magnetic field will pull down on the cantilever, making it harder to deflect, effectively increasing the stiffness. In turn, an anti-aligned field will make the cantilever less stiff. The expression for this effective stiffness taken from the form $F = -k_{eff} \cdot x$ is then

$$k_{eff} = k + |\mu| \cdot |B| \left(\frac{\alpha}{l}\right)^2 cos(\theta_0) \tag{1.9}$$

From there the resonance frequency is given by $f_{res} = 2\pi\sqrt{\frac{k_{eff}}{m}}$ as in any harmonic oscillator, with m the mass of the cantilever.

The extra contribution to the stiffness from the magnetic field is in most experiments expected to be smaller than the inherent stiffness of the cantilever. Using the Taylor expansion of $\sqrt{a+x} = \sqrt{a} + x/2\sqrt{a}$ we get an expression for change of the resonance frequency in relation to the frequency f_0 without a magnetic field

$$f_{res} \approx f_0 + \frac{\pi}{m}|\mu| \cdot |B| \left(\frac{\alpha}{l}\right)^2 cos(\theta_0) \tag{1.10}$$

The important conclusion from this expression is that a linear increase in f_{res} is expected with increasing magnetic field strength, at least for small enough magnetic fields. Also note how a magnetic field in the opposite direction just corresponds to a 180° rotation in θ_0, which introduces a minus sign and instead lowers the resonance frequency of the cantilever with increasing field strength.

In most MRFM experiments, the cantilever can be driven, usually mechanically with a piezo element. This makes the resonance frequency a measurable quantity, taken from deflection response over time. The frequency shift forms the basis of the spin detection of the easyMRFM.

Chapter 2

Device Design

This chapter outlines the design decisions the went into developing the easyMRFM, lists the different elements that make up the device and discusses how they fit together.

The device aims to take the established elements in SQUID-detected MRFM (cantilever with magnetic tip, pick-up loop coupled to cantilever deflection inductively, and SQUID connected to this pick-up loop, method to drive the cantilever) and assemble them in a single probe head. The single-probe-head design allows for flexibility in use and maintaining this flexibility was a guiding principle in the design process.

Earlier efforts in constructing a device like the easyMRFM resulted in the conclusion that the option of optimisation was a necessity to have a realistic chance of getting a workable signal-to-noise ratio. This mainly concerns the coupling between the cantilever and the pick-up loop, which is dependent on their relative position at the micrometer scale (see chapter 3). Therefore, tunability of this coupling became a major design goal.

The device is ultimately meant to operate in ultra high vacuum and at milliKelvin (mK) temperatures in a dilution refrigerator. However, due to the long cooldown and reheating times of dilution refrigerators (several days) and the optimisation process requiring repeated tuning and tweaking, it was decided to make the easyMRFM compatible with dipstick experiments in liquid helium at 4 Kelvin. Using dipstick experiments for the optimisation phase both saves time - two dips are possible in a day - and it reduces the feedback loop time in troubleshooting.

The ultra high vacuum (UHV, $10^{-9} mbar$) in the final easyMRFM setup reduces the damping of cantilever. As explained in the introduction, a very high Q-factor is needed to detect the frequency-shift signal originating from spins in condensed matter systems. An UHV is not achievable

Version of August 30, 2021– Created August 30, 2021 - 14:44

in a simple dipstick experiment, but is instead limited to just a high vacuum (HV, $10^{-3} mbar$). In the optimisation process, however, it is not the frequency-shift response to magnetic fields that needs to be measured, but only the coupling itself. It will be sufficient to drive the cantilever to a large enough amplitude to observe a resonance peak above the noise (see chapter 3). A larger Q-factor of the cantilever is in this instance useful as an amplification of the drive signal, but not necessary for an increase of the frequency resolution which has more strict requirements for MRFM.

This leaves the design with several limiting concerns that need to be taken into account. The probe head needs to be shielded from external magnetic influences. These could either interfere with the deflection of the cantilever, or could be picked up by the loop. A main source of magnetic flux noise are thermal eddy currents in electrical conductors.

Furthermore, thermalisation is a major concern when designing a device at mK temperatures. In a vacuum, all heat dissipation must go through solid heat conductors and the cooling power is limited in dilution refrigerators. Poor heat flow can result in elements not cooling to functional temperatures on any reasonable timescale.

An overview of the device elements can be found in Fig 2.1. A copper structure holds the three chips as the probe head: the cantilever chip, the pick-up loop chip and the SQUID chip. The structure is divided into a the cantilever stage and a SQUID stage that can be moved relative to the cantilever stage with a manual fine-positioning mechanism. The sample stage is separate from the probe head and both can repeatably be disassembled from and reassembled to the cylindrical copper outer shielding.

2.1 Cantilever chip

An IBM-type MRFM cantilever is used, which was developed by Chui et al[13]. This is a soft single-crystal silicon cantilever that is 100 nm thick and has a (constant) width of 5 μm. These cantilevers are produced in three different lengths: 140, 170, and 200 μm, all with resonant frequencies in the range $f_0 = 2 \cdot 10^3 - 3 \cdot 10^3\ Hz$. The spring constants of the IBM cantilevers in our lab have been in the range 50 en 150 $\mu N/m$. Q-factors between $5 \cdot 10^3$ to $10 \cdot 10^3$ have been found at room temperature in high vacuum (see chapter 4), but Q-factors up to $3 \cdot 10^4$ can be expected at mK temperatures in ultra high vacuum[11].

Close to the cantilever tip, the cantilever has a disk shape. In optically-detected MRFM, this functions as a large reflective surface for a laser, but the disk has no function in SQUID-detected MRFM.

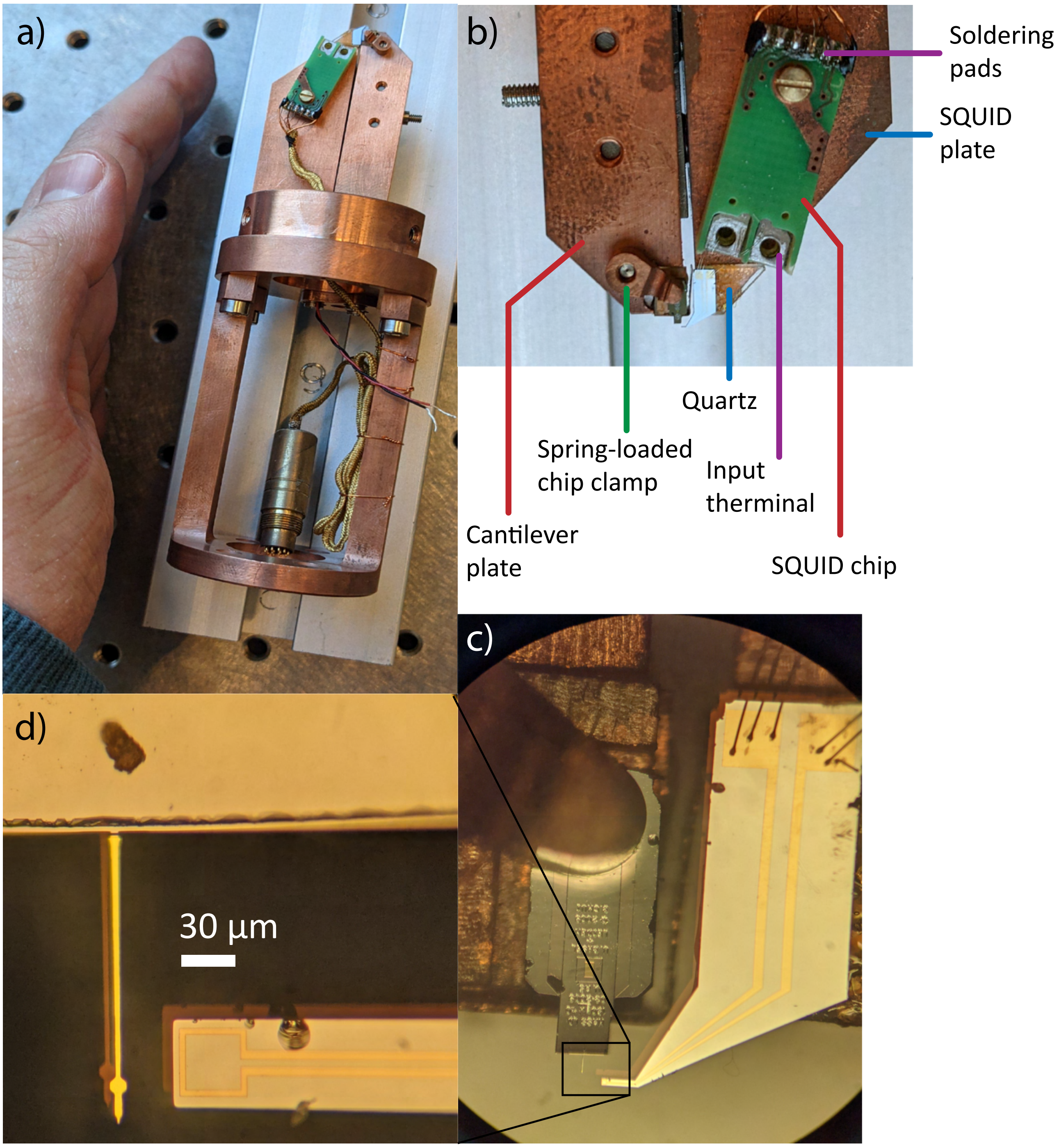

Figure 2.1: ***(a)*** *Overview of easyMRFM, showing the copper supporting structure.* ***(b)*** *Probe head overview, showing the elements on the cantilever and SQUID plates.* ***(c)*** *Mounted cantilever chip (left) and pick-up loop chip (right).* ***(d)*** *Zoom in on the relative positioning between the cantilever and pick-up loop.*

Version of August 30, 2021– Created August 30, 2021 - 14:44

The cantilever itself is attached at the edge of a ~ 1 mm x 2 x 0.3 mm silicon chip. This allows for practical transportation of the cantilever with tweezers. It is the bulky chip that is mounted on the easyMRFM. The chip conducts heat well, meaning the cantilever can be cooled by cooling the chip.

A micrometer-sized magnet is attached at the tip of the cantilever in a SEM using a nanomanipulator. The cantilever tip is approached to $\mathrm{Nd_2Fe_14B}$ powder with spherical particles and one such particle is attached to the tip using Electron Beam Induced Deposition (EBID) of platinum. After the magnet is attached, it is magnetised in the z-direction (along the long side of the cantilever) in a vacuum at room temperature. The magnetic dipole moment $|m|$ can be calculated using the volume of the sphere $V = \frac{4\pi}{3}r^3$ with r the radius, and the saturated residual flux density B_r (remnant magnetisation), which is in the range 1.15 - 1.3 T for $\mathrm{Nd_2Fe_14B}$.

$$|m| = \frac{1}{\mu_0}\frac{4\pi}{3}r^3 B_r \tag{2.1}$$

The exact radius of a tip magnet varies between cantilevers, but is generally around $r = 1.5\ \mu m$. This results in a dipole moment of $|m| = 13$ $A\mu m^2$.

2.2 Pick-up loop chip

SQUID-detected MRFM functions on the principle that the changing magnetic field from the moving cantilever tip can be detected inductively with a pick-up loop. The easyMRFM sets itself apart from previous SQUID-detected MRFM schemes by printing the pick-up loop on a separate chip that can be placed independently from other elements. The silicon chip with native oxides on top, contains the loop and leads connecting to large pads where wire bonds can be set in order to connect the loop to the SQUID chip, which effectively functions as a current sensor. The loop and leads are made out of 100 nm thick NbTiN, fabricated by Delft Circuits [14][15]. Using a superconducting material like NbTiN for the pick-up loop circuit is important because a finite resistance causes losses in the signal and introduces Johnson noise. The critical temperature of NbTiN of 15 K enables dipstick experiments with liquid helium at 4 K. A schematic for the electronics of the pick-up loop circuit can be found in Fig 3.2 in chapter 3, where there is also a full analysis of the effect of the electronics on the signal strength.

The loop itself is square, with the inside measuring 30x30 μm^2. The leads leave with two parallel lines from the middle of the loop with a spacing of 4 μm between them. Other intended measures of the leads were unfortunately lost since the chips were fabricated several years ago, but the known loop dimension could be used to map the distances from optical images. The found approximate dimensions of the leads are drawn in Fig 2.2, not to scale.

Aside from the circuit leads, the shape of the chip also has function. The pick-up loop needs to approach the cantilever possibly up to only several micrometers, so the loop must be very close to the edge of the chip on the approaching side. Additionally, the cantilever is attached in the middle of the cantilever chip, limiting the pick-up loop chip dimensions on the side of the mounting structure when reaching the cantilever. The last edge of the pick-up loop chip is on the side of the sample, where it can not exceed the cantilever tip. Therefore, the loop is printed on a long thin arm that is barely wider than the loop itself. The positioning of the leads varies in the set of fabricated pick-up chips, with some chips having the loop closer to the edge. These can be positioned a few micrometers closer to the cantilever and are the preferred choice.

The inductance of the pick up loop L_L has been measured (probably, by Martin de Wit) to be 4 nH. This is high compared to what could be expected from an approximation using the analytical expression for the inductance of a square loop with circular wire

$$L_L = 2w\frac{\mu_0}{\pi}\left[(\sqrt{2}-1) - ln(1+\sqrt{2}) + ln(4w/d)\right] = 0.1 \pm 0.01\; nH \quad (2.2)$$

with side lengths of $w = 30\ \mu m$, wire diameter $d = 1 \pm 0.5\ \mu m$. A discrepancy of one order of magnitude is significant, so in further calculations, it should be taken into account that the picked up signal might be lower than expected with $L_L = 4$ nH

The leads also has an inductance L_{tr}. This parasitic inductance will not pick up any signal from the cantilever, but still contributes to the impedance of the circuit and will lower the signal in this way. The inductance of the leads can be calculated by adding up contributions from multiple segments in series, marked by colour in Fig 2.2. The red section next to the loop contributes an insignificant amount and can be neglected. The orange section consists of two parallel planes, which has an analytical expression that holds when the thickness of the plane is much smaller than the width (which is actually the same expression as for 2 parallel wires)

$$L_{par} = \frac{\mu_0}{\pi} arccosh\left(\frac{s}{w}\right) \cdot l \quad (2.3)$$

where s is the centre-to-centre distance between the plates, w is the width of the leads, and l is the length of the segment. Taking dimensions from Fig 2.2 for the orange segment $s = 252~\mu m$, $w = 85~\mu m$, $l = 2045~\mu m$, resulting in an inductance contribution of 1.43 nH.

The blue section contains two straight planes with linearly increasing w and s. Furthermore, the planes are of different lengths. To get an order of magnitude approximation, the average length can be taken, as well as the mean w and s over the section. This is somewhat justified because the linearly diverging leads can be interpreted as many small sections of different dimensions in series. The ratio s/w only changes a small amount across the section, from $\sqrt{2(4+4.5)^2}/4.5 = 2.67$ for the small side to $\frac{167+85}{\sqrt{2}}/85 = 2.10$ for the large side (dimensions from Fig 2.2 with the 45 degree angle taken into account). Taking the mean value for the ratio $s/w = 2.39$ and $l = 1558~\mu m$ results in a contribution to the inductance of 0.94 nH.

The total parasitic inductance from the leads on the pick-up loop is then given by $L_{tr} = 1.43 + 0.94 = 2.4$ nH. This is comparable to the inductance of the pick-up loop itself and can not be neglected.

The pick-up loop chips were fabricated on one large wafer and our lab has stored the chips still inside shards of this silicon wafer for the last few years, shielded from light. Breaking out the chips from the wafer without damaging them is more difficult than with other chip designs, because the thin arm is mechanically fragile.

As is usual for chips in wafers, the outline of the chips is cut out with bosch etching, leaving only a thin trace that can break easily. However, some parts of the outline are kept thicker for structural support. While breaking these thick sections, adjacent parts of the chip surface may come off as well. This has turned out to problematic for the loop arm, because of the proximity of the NiTiN leads to the chip edge in this area.

Another point of caution for the chip break out process, is the wire bond pad on the far end of the loop arm. The large thick section of the leads on this side has a tendency to pull away more than half of the wire bond pad. This does not render the chip unusable, however it does hinder the possibility of setting multiple wire bonds.

So far there has been about a 1/5 survival rate in the manual break out process. A combination of broad (~ 2 mm) and thin (~ 1 mm) carbon tweezers were used to push down on a chip or wafer and sometimes grabbing chips from the side to tilt the chip surface on an angle to the wafer.

After break out, the pick-up loop chips can be tested to check their integrity using a 4-point electrical resistance measurement over the whole chip circuit, from pad to pad. Four thin needles on mechanical micro-positioning stages have been used as probes. Intact chips have registered resistances between 10 and 12 kΩ.

The chips in the wafer still have a layer of UV resist on top, as a left-over from bosch etching. This would probably not interfere with the spin detection of the easyMRFM, however it hinders setting the wire bonding on the NiTiN pads. The layer can be stripped using the solvent NMP or similar compounds. In this case the solvent of choice was NEP AR 300-70, which is far less toxic (although still toxic). Do not use a sonicator in any part of the process, because it will destroy the loop arm.

In the end, the following cleaning protocol was used: 1) Submerge the chip in NEP AR 300-70 for 30 minutes at 80°C. 2) Wet transfer and dip into room temperature Acetone. Wiggle the chip around a little to allow the liquid on the chip surface to dissolve 3) Wet transfer and dip into room temperature isopropanol alcohol. Wiggle the chip around a little. 4) Blow dry with N_2 gas.

2.3 SQUID chip

A Superconducting Quantum Interference Device (SQUID) consists of two Josephson junctions in parallel. A supercurrent runs across the device and this current depends sensitively on the flux inside the loop that these two junctions form. In this way, flux can be measured up to fractions of a fundamental flux quantum.

The SQUID used in the easyMRFM is a commercial product fabricated by Magnicon (model: '2-stage Current Sensor C70L116W', colloquial name: 'M', sensor ID: 'C630_G22'). Other models were also available in the lab, but this model fits best with the electronics of the pick-up loop. This is discussed in chapter 3. It is a 2-stage device, meaning that the SQUID junction that initially measures the input flux is read out by a SQUID array that amplifies the signal. Both the single sensor SQUID and the array are shunted and can be flux biased to operate in the most sensitive region in flux-supercurrent phase space.

The signal current to be measured reaches the sensor SQUID inductively via an input coil. This input coil has an inductance of $L_{SQ} = 150$ nH and the mutual inductance between the input coil and the measuring SQUID is $M_{in} = 1.18\ \Phi_0/\mu A = 8.99$ nH. The sensitivity of the SQUID is limited by the internal flux noise, which is a frequency-dependent quantity. The flux noise is $0.36\ \mu\Phi_0/\sqrt{Hz}$ at $1\ kHz$ and $0.28\ \mu\Phi_0/\sqrt{Hz}$ at $10\ kHz$.

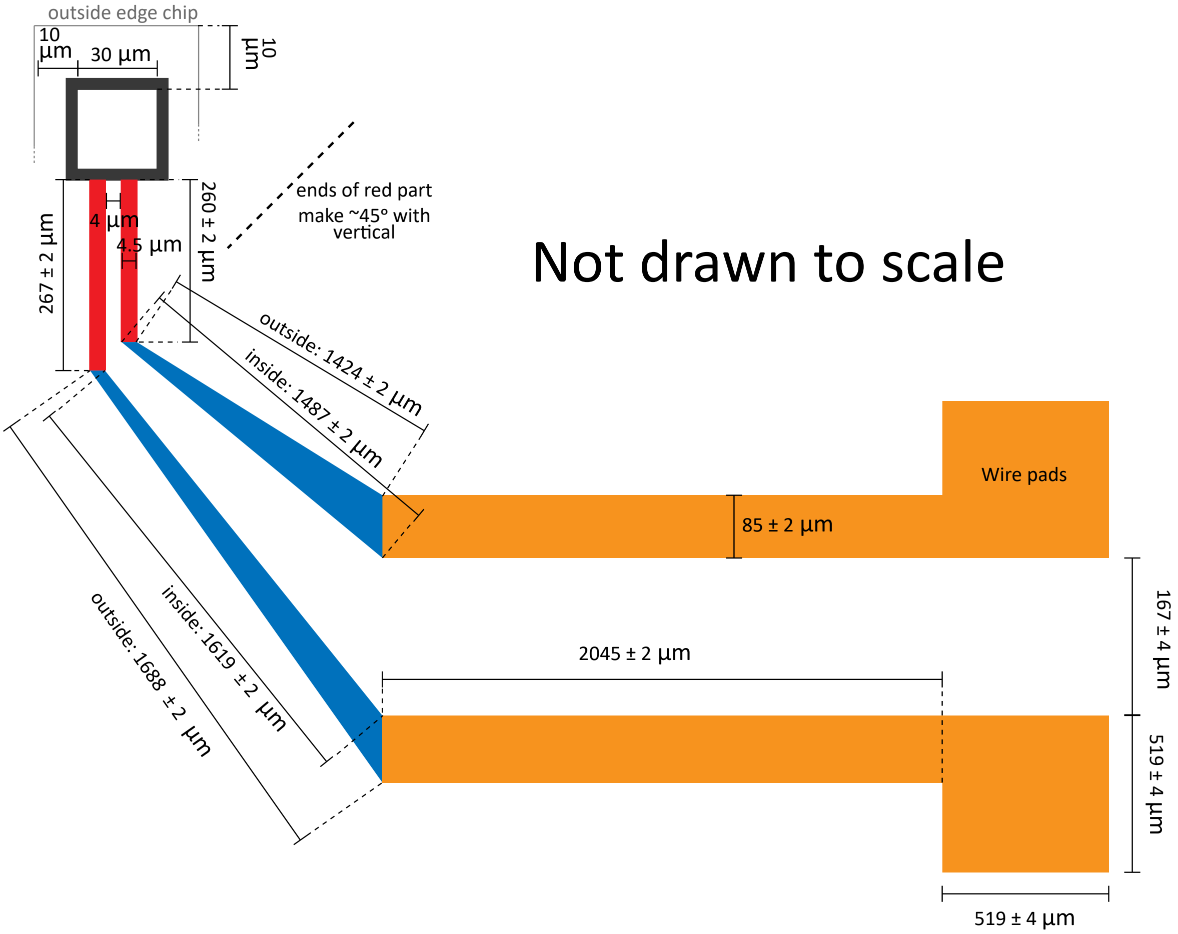

Figure 2.2: *Schematic of the electrical circuit leads on the pick-up loop chip, not to scale, including dimensions that were derived from scale bar in thesis Martin de Wit (fig 9.1c Page 144). Lengths can be off if that scale bar is incorrect. Colours represent regions for the calculation of the induction.*

The superconducting elements of the device consist entirely of NbTi, a superconductor with a critical temperature of 10 K[16], so the SQUID should be operational at liquid helium temperatures. Although the above values for the SQUID properties might deviate slightly, because these have been obtained by Magnicon at 380 mK.

The SQUID is carried by Magnicons CAR-1.2 break-out chip that provides soldering pads for in and outputs. Soldered on is a NbTi cable with a LEMO connector that leads away from the probe head. The flux signal inputs are the exception. These niobium terminals are connected to the pick-up loop chip with wire bonds.

The SQUID signal in the cable can then be interpreted and analysed outside the setup with Magnicons 'XXF-1 SQUID electronics' box. Inside the CAR-1.2 chip, the SQUID chip is connected to the CAR-1.2 soldering pads using niobium wire bonds that were set by Magnicon, again to enable experiments at 4 K. An overview for the mapping from the CAR-1.2 pads to the LEMO connector can be found in Fig 2.3. Only pin 11 is non-standard. It was a single wire unused that would be better off connected than accidentally shorting a circuit. Since the SQUID was already mounted, it was attached to the $-V$ ground. This ground is separate from the $-I/-Fx$ ground in the SQUID chip, but these two are probably connected in the SQUID electronics box. This pin 11 might potentially be problematic though, because there are hints in the documentation that the SQUID electronics box expects only an $-I/-Fx$ input at pin 11.

The CAR-1.2 can be mounted with screw and nut through a single hole in the middle of the chip. This screw also serves as the primary thermal connection to thermalise the SQUID. A note of caution: this screw is also responsible for the structural integrity of the CAR-1.2 chip, which actually consists of 2 separated layers that otherwise are only connected by the niobium wire bonds that should not carry any mechanical load.

Although wire bonds have been used to connect with the pick-up loop, the signal input pads also allow for a screw-on connection. The holes for this screw-on connection for the signal input can also be used to secure the two layers of the CAR-1.2 together. Special anti-static screws should be used for this application.

2.4 Wire bonds

The pick-up loop circuit and the SQUID input are connected by wire bonds, 3 per connection from pad to pad. Initially, these were intended to be niobium wire bonds that would be superconducting in dipstick experiments.

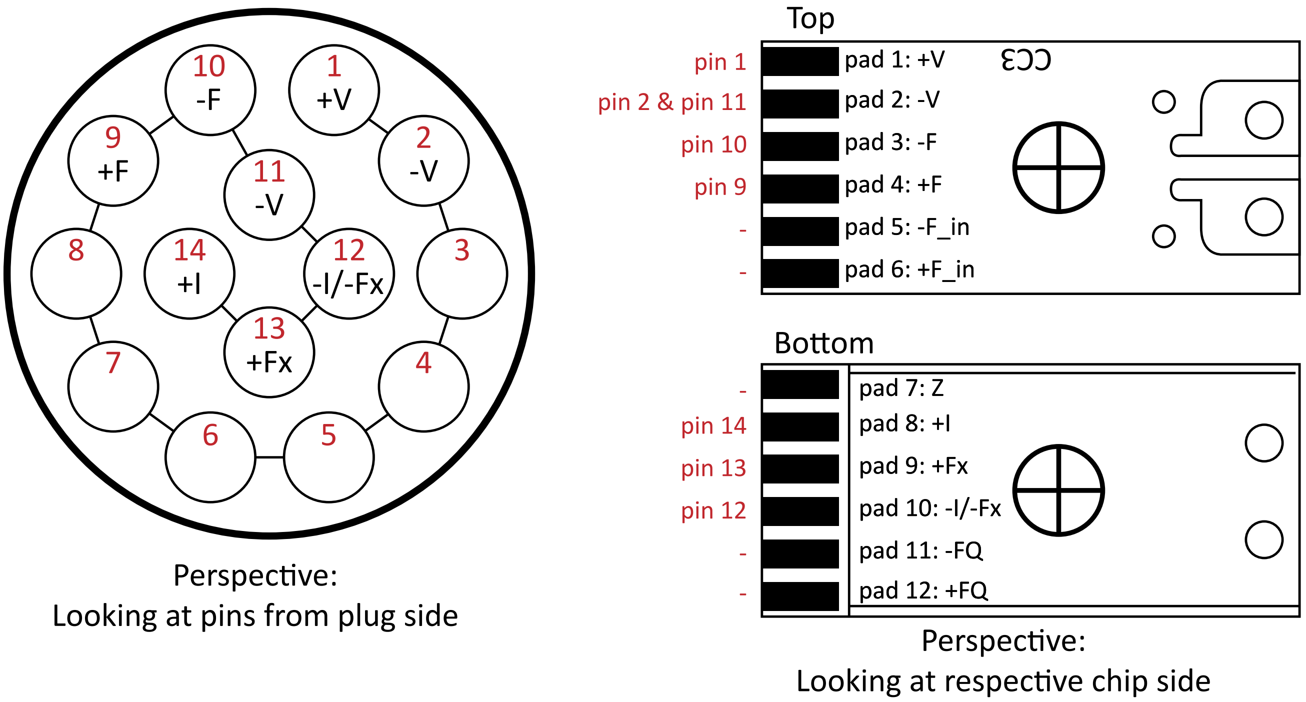

Figure 2.3: *Connections in the easyMRFM between LEMO cable pins and Magnicon SQUID CAR 1.2 chip soldering pads. V is the output for the detected flux signal (amplifier SQUID array), F is the input for feedback on the flux in the sensor SQUID, Fx is the input for feedback on the flux in the amplifier SQUID array, I is input current/voltage over the sensor SQUID. Only pin 11 is non-standard compared to examples in the Magnicon manual.*

A finite resistance in the circuit will introduce Johnson noise that will result in flux noise in the SQUID.

Niobium wire is not trivial to set bonds with. As per the method put forward by Jaszczuk et al[17], the thin niobium wire needs to be annealed before it can be used. If not, the wire will be too stiff to bond by ultrasound vibrations. It is unclear what the annealing process does, either chemically or physically, to make the wire visibly more flexible. We observed that after a few days or weeks, the wires would become stiff again, even when stored in a high vacuum. Our hypothesis is therefore that it is not an oxidation process that causes the stiffness, but rather that there is a change in the crystal grain structure over time.

The company Magnicon, who fabricated the SQUID chip, have found success with this method in their use to make the SQUID chip superconducting at 4K. However, we have found little success in our lab. We suspect a malfunctioning of the wire bonder, but we can not be sure of it yet.

Other superconducting materials have not been tried for wire bonds for the easyMRFM. Lead wire bonds had been considered an option, but no literature on them has been found in the context of using them as superconducting connections. Lead might be too soft for this purpose, or there are issues with oxidation. Furthermore, the company Tanaka used to produce bonding wire from a superconducting alloy, but this production has been discontinued.

The choice was made to use 25 μm diameter aluminium wire bonds instead. Aluminium is a well-established material for wirebonding in superconducting applications. This will come at the expense of introducing Johnson noise in dipstick experiments, because the critical temperature of aluminium is 1.2 K. Chapter 3 discusses the effect of the Johnson noise on the signal and concludes that a driven cantilever will result in a signal above the noise floor in dipstick experiments. The function of the easyMRFM at milliKelvin temperatures will be unaffected by the choice for aluminium wire bonds.

As with the leads on the pick-up loop chip, the wires will introduce a parasitic inductance that will reduce the signal. The inductance of a wire bond can be taken as the self-inductance of a single wire. Using a wire diameter of 25 μm and wire bond length of 4 mm gives an inductance of 4.5 nH for a single pad-to-pad wire bond connection. This is reduced by setting multiple parallel wire bonds per connection, three in this case, which can be approximated by dividing the single wire inductance by the amount of parallel bonds. With two wire bond connections in the circuit, this leads to a parasitic inductance contribution of $(4.5/3) \cdot 2 = 3$ nH.

2.5 Piezo element

To observe the cantilever frequency shift, the cantilever needs to be driven at controlled frequencies. A proven method at milliKelvin temperatures is to vibrate the cantilever chip mechanically with a piezo-electric element[11]. The piezo element used in the setup is the PL022.31 model by PI Ceramic. This is a cubic 2x2x2 mm^2 multiplayer device intended for chip actuation in Ultra High Vacuum environments. While this model is not rated for milliKelvin temperatures, a lower operational temperature should only result in a smaller travel range than the intended 2.2 μm.

The capacitance across the piezo element is rated to be 25 nF at room temperature. In dipstick experiments at 4 K, the combination of piezo and 1m long unshielded copper cables was measured to have a capacitance of only 6.5 nF.

To maximise the mechanical coupling between the cantilever chip and the piezo, the chip is mounted directly on top of the piezo element. The opposite side of the piezo is attached rigidly to the copper mounting structure.

The mechanical coupling to the cantilever is hard to predict. In order to determine the absolute coupling, the setup will have to be calibrated with a different driving method with which the absolute cantilever deflection is known. The thermal motion of the cantilever is a good candidate, although this will be a very small deflection.

2.6 Copper mounting structure and titanium flexture hinge micro-positioning

The chips and piezo of the probe head are mounted on a copper structure that consists of four sections: the cantilever plate, the SQUID plate with the pick-up loop, the supporting structure, and the shielding.

The cantilever plate is the main rigid section of the probe head. The piezo element is mounted in a cut-out corner at the tip of the copper structure. The experiment is shielded from emitted electric field of the AC-operated piezo by two small thin 90°-folded copper plates glued on top of the piezo. The shielding covers the three exposed sides of the cubic cut-out corner.

An acrylic mount for the cantilever chip is glued on top of the piezo (with the shielding in between). A spring-loaded copper clamp is installed next to the acrylic to push down on a mounted cantilever chip.

This method of mounting is not permanent, so one cantilever could be swapped out for another. Furthermore, the cantilever chip can be repositioned within the acrylic mount.

The clamp provides the thermal connection for thermalisation of the cantilever. The strength of the clamp can be adjusted by with a screw on the bottom, however for mounting and dismounting, the clamp should just be lifted up and pushed to the sides.

The SQUID chip and pick-up chip are mounted on the SQUID plate. This section is connected to the cantilever plate via two titanium mechanical micro-positioners that each can move the SQUID plate relative to the cantilever plate independently along the x and y-axis.

At the tip, the pick-up loop chip is glued on top of a pure quartz piece, that itself is glued to the copper plate. The chip is not attached to the copper directly in order to avoid the flux noise induced into the circuit by thermal electric eddy currents in the copper bulk. Quartz is an electric insulator, but does conduct heat well at milliKelvin temperatures because of phonon-mediated heat transport.

As mentioned in the section on the SQUID chip, it is mounted on the copper with a screw and a nut. The niobium flux input terminals should be as close as possible to the wire bond pads of the pick-up loop chip, in order to reduce the wire bond length, which in turn reduces the parasitic inductance. Due to a design flaw in the SQUID plate, the hole for the SQUID mounting screw could not be placed at the ideal location, where the SQUID chip would lay flat against the quartz surface. Instead, the chip is rotated.

The single piece micro-positioning mechanism is based on a flexture hinge design, where the tightening of a screw continuously deforms thin parts of a solid structure resulting in axial strain of the bulk piece. Although the screw turns do not linearly translate to displacement. The range of motion of the SQUID plate is about half a millimeter on both axes and is demonstrated in Fig 2.4. It has been found that the reasonably achievable resolution of the hand-operated mechanism is at least 5 μm.

The positioning stage is critical, because the coupling between the deflection of cantilever and the pick-up loop depends on their relative positioning. The ideal positioning is discussed in chapter 3, where it is found that the flux coupling does vary significantly at a micrometer scale.

The positioning set at room temperature will not translate directly to colder operational temperature, however, due to thermal contraction. As a rough estimate, with the thermal expansion coefficient for copper of 16.5 $\mu m/K \cdot m$ (at 25°), a distance of 1 mm will contract 5 μm. With the complicated copper structures, the exact thermal contraction is hard to predict, but it will be relevant.

This is where the tunability of the easyMRFM comes in. The positioning can be optimised by measuring and adjusting the coupling. The measuring will have to be done at operational temperatures for the SQUID, and adjusting will have to happen at room temperature under an optical microscope by hand. Measurements can be performed twice a day with liquid helium dipstick experiments, so, all else functioning, the optimal positioning can be found within a month in the most pessimistic scenario.

While there is a fine positioning stage in the x,y-directions, there is no dedicated mechanism for aligning the z-direction. The SQUID plate is not entirely rigid in this direction, though. There is clearance in the screw-on connection between the SQUID plate and the first titanium positioning piece. This is very much not a precise method and it risks breaking the pick-up loop arm, but it can be done with these screws slightly untightened.

The main thermal connections to the SQUID plate are the titanium positioning stage and the electronic cable to the SQUID chip. These are both not ideal and if problems arise in a dilution refrigerator environment, a slack connection to the cantilever plate can be considered.

A small, already existing connection comes from the protruding copper shielding plate of the piezo, that hits the SQUID plate when in close proximity. This does not hinder the approach with the positioning stage, but could transfer some of the vibration motion to the SQUID plate. The results of this might actually be positive, as y-motion due to the piezo might be better synchronised between the SQUID and cantilever plate, reducing the effect of possible vibrational noise on the pick-up loop/cantilever positioning.

The cantilever plate is attached tightly to the supporting structure, which in turn can be repeatably attached to and detached from the end of a dipstick. The connection between the supporting structure and the dipstick structure is the main point of thermal connection between the cooling liquid helium and the experiment, because the experiment will be operating inside a vacuum tube. This surface of the supporting structure needs to be kept free of oxides in order to optimise the cooling power to the experiment. The heat flow through this connection will not be very good regardless, because the dipstick is made from stainless steel, which is not a good heat conductor at 4 K. Additional thermal connections might be necessary in the future. An option is to use flexible copper connections to the inside of the vacuum tube, which is in direct contact with liquid helium during a dipstick experiment.

The cantilever and SQUID plates are shielded by a copper cylinder around the experiment, attached at the supporting structure. The sample stage will be connected at the other open end of the shielding cylinder, where the the probe head can be reached. The shielding cylinder will also act as the thermal connection to the sample stage. Care should be taken to keep the copper surfaces free of oxides for these connections as well. In a dipstick experiment, the experiment will also be magnetically shielded by the vacuum tube that is covered by niobium foil.

2.7 Sample stage

The sample stage consists of a copper arm where the sample can be attached to. It can approach the probe head in the z-direction with a slip-stick piezo motor. The slip-stick positioner used is the CBS10-RLS model from JPL Innovations. This actuator is rated for milliKelvin temperatures and UHV. Additionally, it is equiped with a Resistive Linear Sensor (RLS) that can be used to determine the absolute travelled distance of the slip stick motor.

On the electronics side, there is a corresponding control module to operate the actuator and take steps. However, there is no read out module for the RLS. In previous SQUID-detected MRFM setups, the cantilever-sample distance has been determined by the increase of the measured cantilever deflection signal as the sample approached with the pick-up loop printed on it. This scheme will not work with the easyMRFM, with a single probe head design. Instead, the idea has been to use the growing capacitance between the probe head and the sample as a measure of distance. If this does not work out, it might be an option to invest in the RLS controller, or reverse engineering the resistance-to-travel distance encoding in a lab-made electronics setup.

The copper arm of the sample-approach stage ends on a flat surface for a sample, but can be swapped out for an arm that has a mount for an electromagnet coil. In the future, this arm will be used for the B_0-field coil in magnetic resonance experiments. More on that in chapter 5.

No sample has yet been mounted on the sample stage, so the technical details on sample preparation are still undecided on.

2.8 Assembly

This section will cover many practical aspects and details of the assembly process, so they can be repeated specifically by research group members.

Version of August 30, 2021– Created August 30, 2021 - 14:44

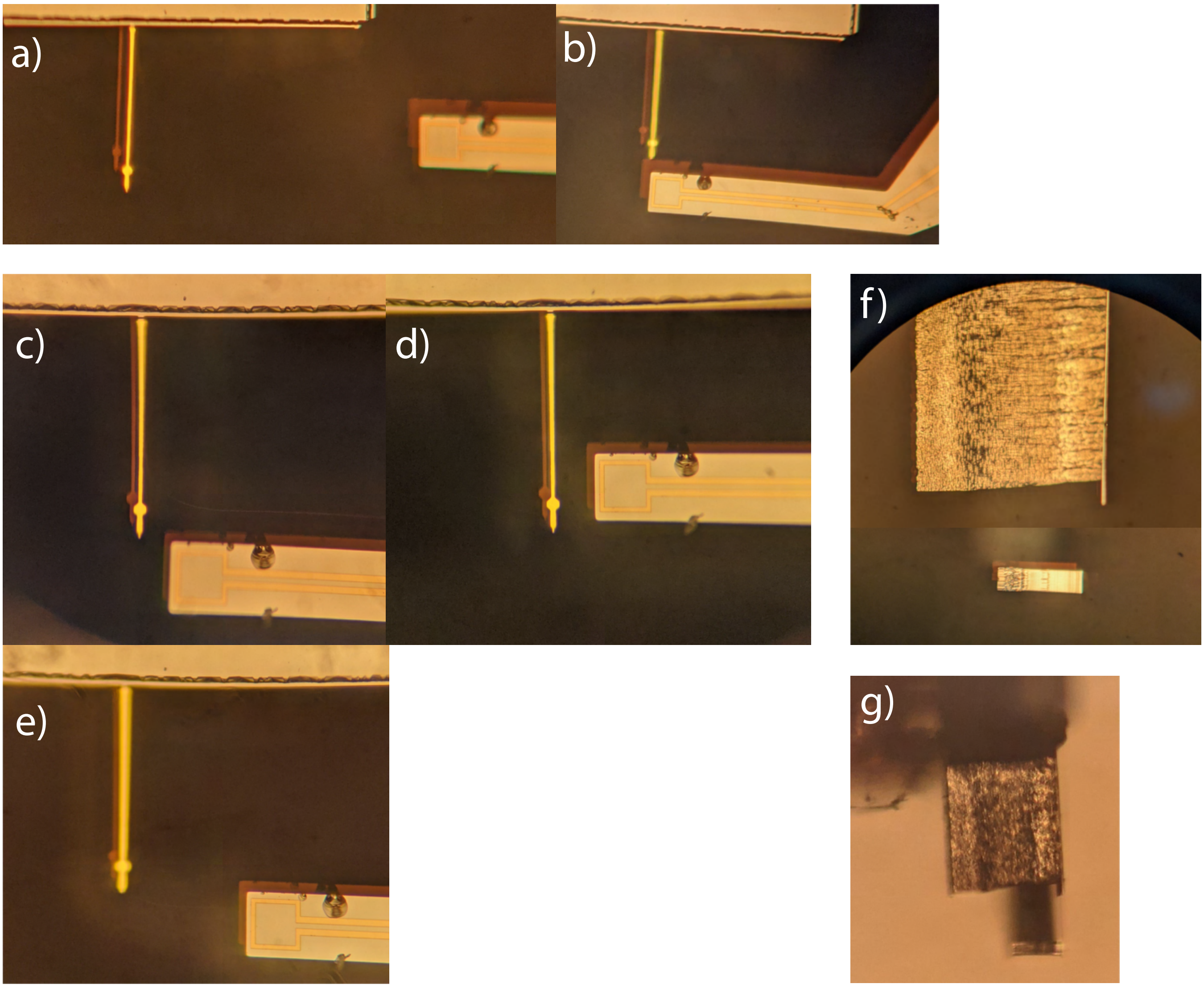

Figure 2.4: *A collection of cantilever and pick-up loop positions.* ***(a)*****-*****(b)*** *exemplify the maximum range of the flexture hinge in the y-direction. The loop can be moved continuously from one to another.* ***(c)*** *and* ***(e)*** *demonstrate the same at a smaller scale. Still with continuous motion, but at this scale less monotone as a function of screw turning in the flexture hinge.* ***(c)*****-*****(d)*** *show that z-positioning is possible, although this is not a controlled easily reproducible motion, since it relies directly on the clearance in the screw connection between SQUID plate and flexure hinge. This must be done by hand and is not geared in any way. Still, with stress and patience, the z-position can be set.* ***(f)*** *and****(g)*** *demonstrate x-alignment. The small depth of focus of the optical microscope hinders precise positioning because the chips are separated in the y-direction. (f) is a composite figure of two magnified images, with the focus shifted between them. (g) just uses a smaller magnification with larger depth of field.*

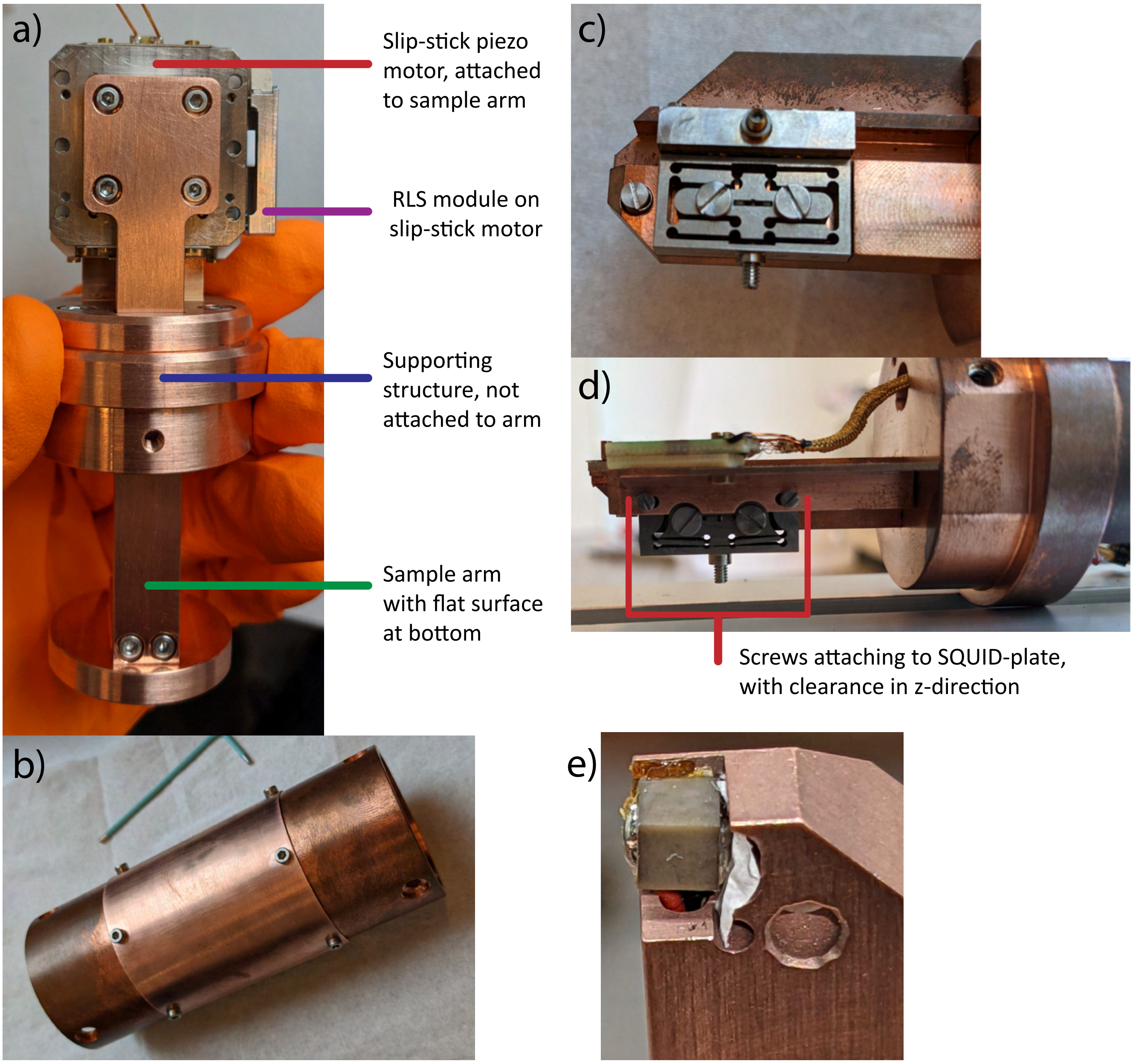

Figure 2.5: ***(a)*** *The 1-dimensional sample approach stage, employing a slip-stick motor.* ***(b)*** *The shielding cylinder, with removable side window to exchange samples without further disassembly.* ***(c)*** *Titanium flexure hinge* x, y*-positioning stage for the SQUID plate.* ***(d)*** *shows how these two elements are attached with two screws. There is clearance in the* z*-direction (useful), but also in* x*.* ***(e)*** *Mounted piezo element (glued to back side), before covered up by shielding plates. Metallic blobs on the side are soldered wire connections that run down through the cantilever plate. White sheet is insulating blotting paper.*

GE varnish has been used as a glue in all cases, because of the high thermal conductivity and small thermal contraction. At least 24 hours were waited before gluing any element on top of any other glued element. If needed to be removed, the glue can be dissolved in ethanol.

The copper structure of the easyMRFM is cylindrical. It is easiest to work on the device with the cylinder on its side. Being able to freely rotate the cylinder is useful when working on the device, so the best mount for the assembled easyMRFM is some heavy object with a groove of a few centimeters wide that prevents the device from rolling away.

On the cantilever side, the first element to be glued to the copper structure is the piezo. The glued sides are electronically isolated from the copper structure by a piece of blotting paper in the glue layer. The thin copper shielding plates were glued over the piezo. The first directly on the piezo, with again a piece of blotting paper in between, covering the exposed z and x-directions. The second was glued to the first shield at the z side, without blotting paper, and covers the exposed y direction towards the SQUID as well.

The cantilever acrylic mount is glued on top, The cantilever mount should be aligned straight with the larger copper cantilever plate. After inspection, it turns out the mount is $\sim 1.5^\circ$ turned clockwise. When placing the cantilever chip later, this should be taken into account.

Concerning the titanium flexure hinges: it was found that they were easiest left attached to the cantilever stage. The SQUID plate is attached to the y-axes stage with two screws that are accessible when the easyMRFM is rolled with the chip surface is pointing slightly above entirely sideways. In this position, the SQUID plate can rest on the corner between the plate and its shallow fin on the bottom. The SQUID plate is quite light. When it is not attached, it is useful to clamp it on its fin on a heavy vice.

This is especially the case when the SQUID chip is soldered to the SQUID cable that runs through a hole in the support structure where the plug on the other side doesn’t fit through, and the SQUID plate can not be far removed from the main structure.

On top of the SQUID plate, the quartz piece should be glued in the designated cut out part at the tip. The current piece of quartz is actually slightly too wide for the copper and sticks out on the diagonal side in order to keep the space between the two sides empty so they can approach as close as possible.

The SQUID cable must run through a hole in the main support structure. The plug on the other end of the cable does not fit through that hole, so it is important to have the cable run through the hole before soldering. Originally, the SQUID cable was soldered to the chip before it was attached to the plate. This was preferable because with the SQUID screwed tight, the bottom soldering pads are less accessible. However, our electronics technician has succeeded in setting a new cable while the chip was attached to the SQUID plate.

After the cable is connected, the SQUID plate can not be removed far from the supporting structure. The use of a heavy vice for the SQUID plate is even more recommended in for this situation, because it is very easy for a moving cable to throw around the SQUID plate and break things.

As it is now, removing, or even moving the SQUID chip should probably not be done any time soon, because of the risk of breaking the niobium wire bonds between the two layers of the CAR chip. If it needs to be removed, the anti static screws should be added on first on the input pads.

When soldering on the SQUID chip, read the instructions on the limitations. For example, there are limitations on the heat and you should always be mindful of static electricity that can wreck the weak link Josephson junctions.

With the SQUID chip attached and ready, the next step is mounting the pick-up loop chip, which will involve first mounting a cantilever chip (assuming both have been prepared as mentioned in their respective sections 2.2 and 2.1). To start, the SQUID plate should be attached to the cantilever plate. Make sure it is screwed tight in the position with the SQUID plate as far down towards the sample (z-direction) as possible. This will help with z-alignment, because it is easier to move the plate upwards then downwards. Also make sure the y-direction flexure hinge is positioned with the SQUID plate as far a possible from the cantilever side. This will help with not breaking the cantilever or loop by avoiding contact while gluing.

Then, the cantilever chip should be mounted. It will serve as a reference for placing the pick up loop. Preferably, this could be a broken cantilever chip (there are many). It is probably best to do the cantilever mounting by eye only, and not use a microscope.

Lift up the clamp with tweezers and set it aside on the edge of the acrylic. Pick up the cantilever chip with 1 mm tweezers to lay it down on the acrylic, most likely only partly on the mount. Take up metal thin tweezers to move the cantilever chip in position. As can be seen in Fig 2.1c, the cantilever chip should not touch the outside edges of the acrylic. For the z-direction, this is useful because it provides a buffer to correct the z-alignment in the other direction than the clearance of the SQUID plate. For the y-direction, it is actually needed to have the pick-up loop reach the cantilever, because the loop arm is just a little short. It also makes it easier to pick the cantilever chip back up again later.

Lift the clamp from the acrylic edge and bring it down on the cantilever chip. The cantilever chip can be rotated under the clamping pin, but only barely pushed. Make sure the chip is aligned straight with the edge of the copper structure, not the acrylic mount. For major adjustments, the clamp should be lifted back up again.

The next step will be to mount the pick-up loop chip with glue. The positioning of this chip will be critical, however not too much time should be taken to adjust as the GE varnish is drying. Too many adjustments made while the GE varnish is dried to a more viscous state, will lead to the chip not adhering to the quartz and detaching when dry. Another important factor in adhesion is that the quartz surface should be clean. Especially glue remains have been shown to be detrimental.

The location of the pick-up loop chip on the quartz should be as close to the cantilever side as possible for the y-direction. The loop arm needs to be overlapping with the cantilever chip already in order for the loop to be in range for an approach with the flexure hinge. In the z-direction, the position of the loop relative to the cantilever tip is leading. They should be at the same height, but remember it can still be adjusted later. The chip will probably hang a little over the edge of the quartz at the wire bond pads. This is fine, but too much overhang and the chip can break during wire bonding (the same is true for the y-direction). The chip slightly rotated counter clock-wise would be preferable over clockwise. In this way the loop approaches the cantilever tip from the side away from the sample. This prevents the pick-up loop chip having any part closer to the sample than the cantilever tip.

For the gluing process, take three wooden q-tips. Sharpen the wooden side of one. Use one q-tip to take out a big droplet of GE varnish. Use a second q-tip to scrape a good medium droplet of GE varnish from the first q-tip and deposit it on the quartz surface. Use the sharpened wooden side to spread the glue. Pick up the pick-up loop chip with broad tweezers and place it. Adjust the chip position broadly with a thinner set of tweezers and the wooden point.

Only now move the device under the optical microscope to look at the z-alignment and adjust. When satisfied with the chip position, take clean broad tweezers and push down gently yet firmly on the chip. Try to finish the whole process in only a couple of minutes and then let it dry.

When working the glue-stained tools, make sure that they are always discarded on the pick-up loop side and are not moved above or across the cantilever chip. Glue threads might trail down from these tool and since they are sticky, they tend to break the otherwise quite flexible cantilevers.

With the glue dry, it can be checked whether the loop is close enough to the cantilever in the y-direction. In order to have both the loop and cantilever in focus under the microscope, first align in the x-direction. If the loop is close enough, the next step will be wire bonding. The SQUID plate will need to be removed and clamped in a vice in order to access the bonding pads on a stable surface straight from the top with the strong force of a bonder needle.

After checking, move the loop as far away from the cantilever side as possible and then dismount the cantilever chip. With the cantilever chip removed, there is less risk of the loop arm snagging on it. Thin metal tweezers will be needed, because there is not enough space for any larger. The issue with using the metal tweezers for picking up the chips, is that they chisel the edges of the silicon. This is more of problem for the pick-up loop chip, because there is the actual risk of destroying the circuit on the surface.

Hold the SQUID plate while unscrewing it. An extra pair of hands can make it less stressful. After wire bonding, the SQUID plate can be reattached. This is more stressful. An extra set up hands is a must to hold the SQUID plate stable in front of the screw thread and simultaneously holding the entire rest of the device stable, while the other person turns the screws.

The cantilever chip can be mounted again in the same way (must be the intact version this time). The loop should be positioned to the intended location now. Even though there are few other options, it is risky to do the z-alignment by using the clearance of the screws to the positioning stage.

Chapter 3

Models for the cantilever deflection signal

Multiple numerical and analytical analyses were done on the cantilever and pick-up loop system to estimate the expected signal in the SQUID. The results of these models were used mainly to check for feasibility and to guide some of the design decisions.

One of the topics discussed in this chapter is the dependence of the coupling between the cantilever and the pick-up loop on their relative position. It is this position that can be varied in the device in order to optimise the coupling.

Other results include the flux coupling between the pick-up loop and the SQUID. The parasitic inductance in the pick-up loop chip circuit reduces this coupling. The option of using a transformer is considered. Furthermore, the effects of a finite resistance in the otherwise superconducting circuit are investigated, specifically to investigate the possibility of aluminium wire bonds.

3.1 Coupling between the cantilever and pick-up loop

The pick-up loop detects the cantilever deflection inductively. The coupling between the nanomagnet dipole attached to the cantilever tip and the pick-up loop can be investigated by looking at the magnetic flux Φ_L through the loop. The magnetic field $\vec{B}_{tip}$ from the dipole at the tip causes a flux through the surface of the pick-up loop and this flux will change as the cantilever tip moves. The coupling can then be defined as the flux change per nanometer cantilever deflection $C_{CL} = \partial \Phi_L / \partial x$. Using Stokes theorem, this can be rewritten to the line integral of the vector potential $\vec{A}_{tip}$ along the the edge of the pick-up loop.

$$\Phi_L = \int \vec{B}_{tip} \cdot d\vec{a} = \int (\vec{\nabla} \times \vec{A}_{tip}) \cdot d\vec{a} = \oint \vec{A}_{tip} \cdot d\vec{l} \tag{3.1}$$

Because the pick-up loop is much larger (30x30 μm^2) than the tip magnet length ($\approx 1.5 \mu m$), the tip magnet can be approximated by a perfect magnetic dipole with a dipole moment $\vec{m}$. The vector potential for a perfect dipole is

$$\vec{A}_{tip}(\vec{r}) = \frac{\mu_0}{4\pi} \frac{\vec{m} \times \vec{r}}{r^3} \tag{3.2}$$

where μ_0 is the vacuum permeability and $\vec{r}$ is the position relative to the centre of the dipole. As explained in section 2.1 of chapter 2, the the dipole moment is pointing in the z-direction and can be assumed to have a magnitude of around $|m| = 13\ A \mu m^2$.

From there, the coupling can be calculated for a range of different cantilever positions $\vec{r}$. 2D slices taken from the full 3D mapping of the coupling strength can be found in Fig 3.1.

It can be observed in Fig 3.1a that the z-position of the cantilever should be a little lower than the loop for optimal coupling. This is convenient, because it is required that the cantilever is closer to the sample than the loop, to avoid touching the pick-up loop with the sample. From Fig 3.1a and b, it can be concluded that the y-position of the cantilever should be as close to the loop as possible. However, a possible snap-to-contact should be avoided, where the cantilever attaches itself to the pick-up loop chip due to electrostatic forces. This limits the relative y-position to an conservatively estimated $y = 45\ \mu m$, although this could be lowered by experimenting at which distance snap-to-contact occurs in practice.

In Fig 3.1b it can also be observed that x-position should be right at the middle, at $x = 0\ \mu m$. This can then be combined with the $y = 45\ \mu m$ to find the optimal $z - position$ in Fig 3.1c. The visible 10 μm-sized blob in red centers around $z = -25\ \mu m$, where it corresponds to a coupling of 150 $\mu \Phi_0 / nm$.

The mechanisms for alignment in the x and y-direction have been shown to be able to reach the required positions within fewer than 10 μm, however the lack of precision alignment mechanism for the z-direction makes it doubtful that this optimal 150 $\mu \Phi_0 / nm$ can be achieved. Still, the loop

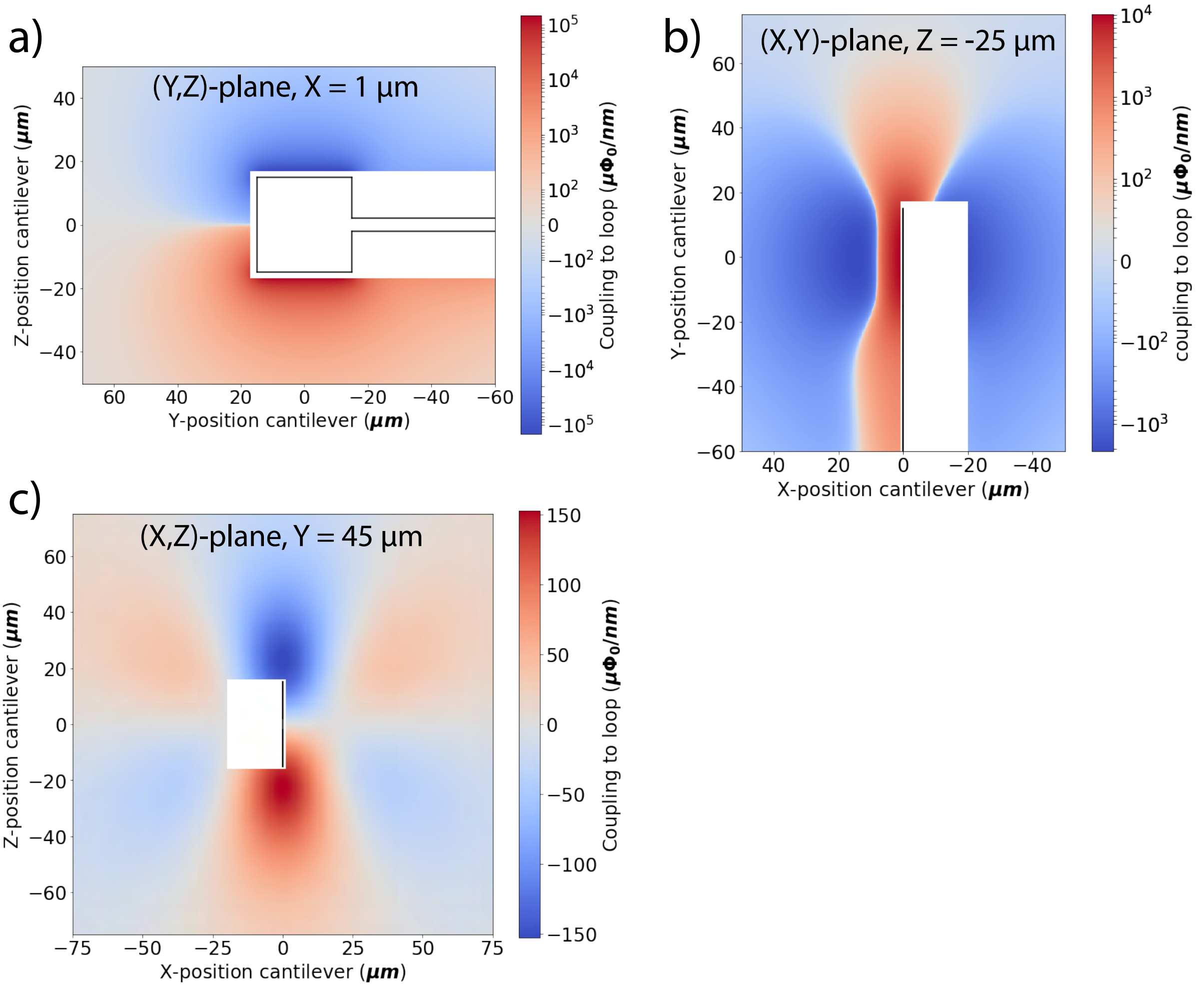

Figure 3.1: *The modelled inductive coupling C_{CL} of the cantilever deflection to the pick-up loop for different relative positions, in micro flux quanta ($\Phi_0 = h/2e$) per nanometer (nm). Two-dimensional slices are shown in* ***(a)****,* ***(b)****,* ***(c)****, with different orientations. The pick-up loop circuit is illustrated as a black lines on a white body that corresponds to the chip. Note the symmetrical logarithmic colour scales in* ***(a)*** *and* ***(b)****, but the linear scale in* ***(c)****. The positive and negative sides of the logarithmic scales are bridged by a linear part from -50 to 50 $\mu\Phi_0/nm$.*

position showcased in the assembled easyMRFM is comparable, although maybe less consistently reproducible (chapter 2, Fig 2.4c-e). Therefore, based on the achieved positioning in assembly, an expected coupling of at least 100 $\mu\Phi_0/nm$ seems reasonable.

The next step in the analysis of the expected signal is to calculate the peak-to-peak flux difference $\Delta\Phi$ of the oscillation of Φ_L over time as the cantilever is driven, which is given by twice the deflection amplitude multiplied by C_{CL}. This amplitude is determined by the mechanical coupling between the driving piezo element and the cantilever. As discussed in chapter 2, this mechanical coupling will be an unknown factor. Furthermore, the mechanical drive at the resonant frequency will be amplified by the Q-factor of the cantilever. Experiments with other MRFM setups in our group with similar driven cantilevers mounted on top of piezoelectric vibrators have shown an amplitude of 100 nm can be expected (although not necessarily used)[11][12]. This amplitude can be even larger, although at some point nonlinearities in the vibration are introducted. A cantilever amplitude of 100 nm corresponds to $\Delta\Phi = 20\ m\Phi_0$ in the pick-up loop.

3.2 Coupling between pick-up loop and SQUID

The flux change in the pick-up loop induces a current in the circuit of the pick-up loop chip. A schematic of this circuit can be found in Fig 3.2a. This circuit is in series with the input coil of the SQUID chip, where the same current induces a flux that is measured over the Josephson junctions in the SQUID, so the pick-up loop circuit acts as transformer of the flux. The circuit is superconducting, so no resistances are present.

The flux in the SQUID must be larger than the noise floor of the SQUID used for detection. There are several commercial SQUID chips in the possession of our group, all from the manufacturer Magnicon. Their noise floor, the mutual inductance M_{in} between the SQUID input coil and the SQUID Josephson junction circuit inside, and the inductance of the SQUID input coil L_{SQ} have well-defined specifications for all of these models.

The transformation of the flux in the loop Φ_L to the flux in the SQUID Φ_{SQ} can be characterised by a coupling factor C_{LSQ}.

$$C_{LSQ} = \frac{\Phi_{SQ}}{\Phi_L} = \frac{M_{in}}{L_{tot}} \tag{3.3}$$

where M_{in} is the mutual inductance between the SQUID input coil and the SQUID Josephson junction circuit inside, and L_{tot} is the total inductance of the pick-up loop circuit.

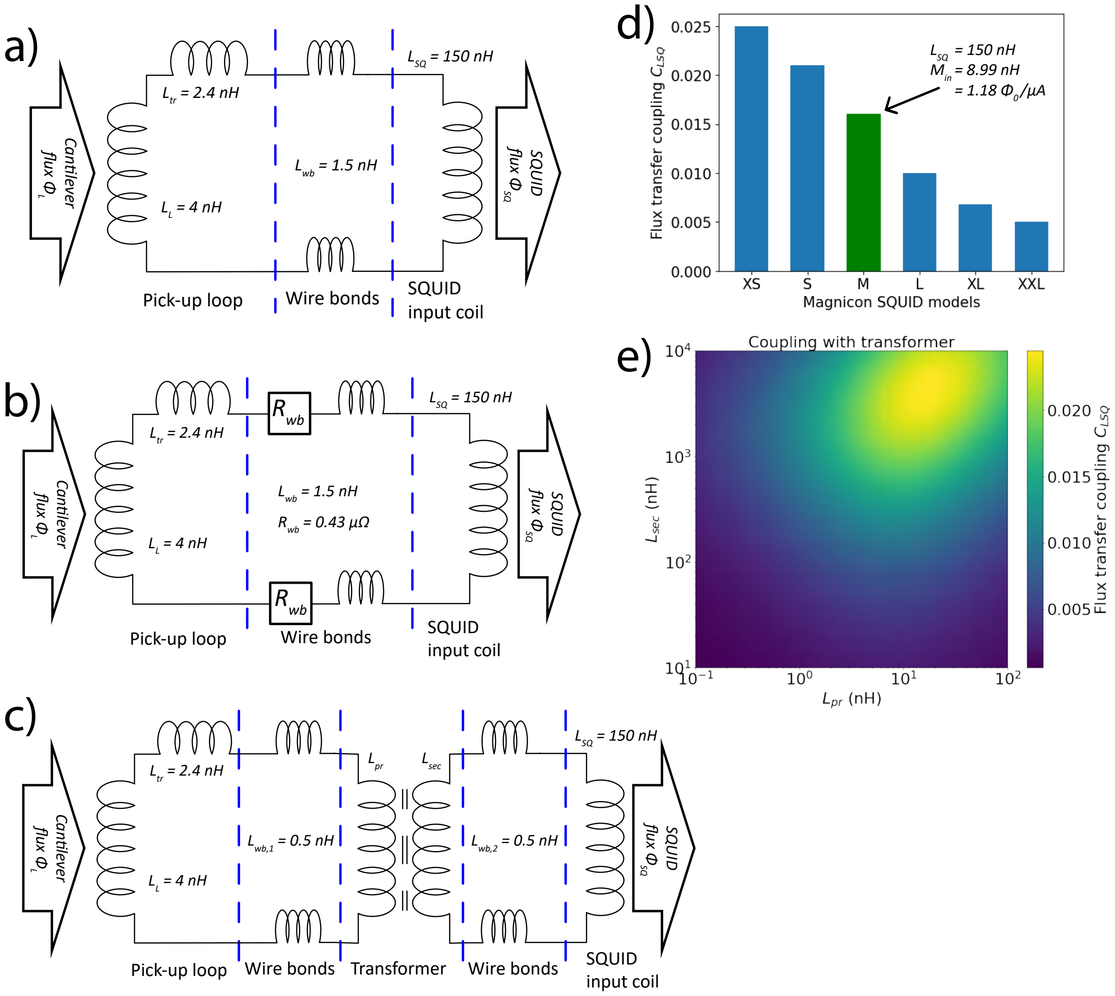

Figure 3.2: ***(a)*** *Schematic representation of electronics in the pick-up loop circuit to the SQUID input coil as assembled, at temperatures where the aluminum wire bonds are superconducting and no resistances are present. The inductances of the pick-up loop (L_L) and SQUID input coils (L_{SQ}) are labelled, as well as the parasitic inductances of the pick-up chip leads (L_{tr}) and the individual wire bond connections (L_{wb}).* ***(b)*** *shows the same circuit, but at temperatures where the wire bonds have finite resistances ($R_{wb} = 0.43$ μΩ per connection) while other circuit elements are still superconducting.* ***(c)*** *shows a hypothetical circuit where a transformer chip, with primary and secondary inductances L_{pr} and L_{sec}, connects the pick-up circuit and the SQUID chip.* ***(d)*** *lists the flux transfer coupling C_{LSQ} of several Magnicon SQUID chip models. The model used in the easyM-RFM is marked in green ('M'), with the corresponding values for L_{SQ} and the mutual inductance to the SQUID M_{in}.* ***(e)*** *shows the calculated C_{LSQ} for a range of values for L_{pr} and L_{sec} in the transformer of the circuit in (c).*

The largest contribution to L_{tot} generally comes from the SQUID input coil. This inductance can be added up with the inductance of the pick-up loop L_L, because they are in series. Furthermore, there are parasitic inductances originating from both the shape of the leads on the pick-up loop chip (L_{tr}) and the wire bonds that connect the pick-up loop chip with the SQUID input coil on the SQUID chip (L_{wb}). This parasitic inductance is also in series in the circuit and can be added up as well. Values for these inductances ($L_L = 4$ nH, $L_{tr} = 2.4$ nH, $2 \cdot L_{wb} = 3$ nH) are discussed in chapter 2.

Fig 3.2d shows the flux transfer coupling factors C_{LSQ} for different Magnicon SQUID chip models. It is evident that the 'smaller' SQUID chips have better coupling. This is mostly due to their smaller L_{SQ}. The smallest Magnicon SQUID chip available in our group at the time of assembly was the 'M' model, so this one is used in the easyMRFM, resulting in an expected flux coupling of $C_{LSQ} = 0.016$.

This result can be combined with the flux difference from the cantilever found in the previous section to get the total flux entering the SQUID: 0.32 $m\Phi_0$. This far exceeds the flux noise level in the 'M' SQUID-model, which is only 0.3 $\mu\Phi_0/\sqrt{Hz}$ around the resonance frequency of the cantilevers ($\sim$3 kHz).

3.3 Coupling to SQUID with a transformer

Because the pick-up loop and the SQUID input coil are not impedance matched, the flux is not transferred as efficiently as possible. A transformer could be used to separate the circuits and match their impedance, like in the circuit shown in Fig 3.2c. The transformer has primary and secondary inductances L_{pr} and L_{sec} in the two coils, which need to be chosen correctly to maximise the coupling C_{LSQ}. In practice, the transformer will be on a separate chip, which introduces a second set of wire bond connections. On the other hand, this transformer chip could be better positioned on the mount than the current mounting of the SQUID chip and reduce the length of the wire bonds to an estimated 1 mm, lowering the parasitic inductance.

In a transformer circuit, the flux transfer coupling is given by

$$C_{LSQ} = \frac{M_{12} M_{in}}{L_1 L_2 - M_{12}^2} \tag{3.4}$$

where $L_1 = L_L + L_{tr} + 2 \cdot L_{wb,1} + L_{pr}$ and $L_2 = L_{sec} + 2 \cdot L_{wb,2} + L_{SQ}$ are the total inductances of the two separated circuits and M_{12} is the mutual inductance of the transformer, given by

$$M_{12} = k \cdot \sqrt{L_1 L_2} \tag{3.5}$$

where k is a coupling constant between 0 and 1 that defines the efficiency of the transformer. In previous SQUID setups with transformers, it was found that transformers on chips could reasonably reach $k = 0.9$ or even higher, so this value is chosen in this analysis.

The flux-transfer coupling can be calculated for a range of L_{pr} and L_{sec} to investigate the highest possible coupling. The results of this can be found in Fig 3.2e. There is a clear optimal combination for L_{pr} and L_{sec} where the C_{LSQ} is a maximal 0.024. It can be concluded that the addition of a transistor can only improve the flux coupling by less than a factor of two. As we were not in the possession of a transformer chip with the optimal induction properties and the calculated signal-to-noise ratio without a transformer was already sufficient, no transformer chip was included in the design.

3.4 Coupling to SQUID with aluminium wire bonds

As discussed in chapter 2, the easyMRFM was designed to operate both at mK temperatures, as well as liquid helium temperatures. To this end, all electrical elements in the pick-up loop circuit and the SQUID are made with niobium and niobium alloys, which are superconducting at 4 K. The exception to this are the aluminium wire bonds that are only superconducting at 1.2 K. While niobium wire bonds have been realised by others [17], it proved more difficult in practice and there had to be defaulted to the standard choice of aluminium for superconducting wire bonds.

This choice has no consequence on the coupling at mK temperatures. In this case, the entire circuit is still superconducting and the analysis in section 3.2 applies. However, at 4 K the wire bonds will introduce a finite resistance in the circuit. The resulting circuit can be found in Fig 3.2b. An estimate of the resistance of a single aluminium wire bond can be made from the bulk resistivity at 4 K, $\rho(T = 4K) \approx 1.0 \cdot 10^{-13}\ \Omega m$[18]. A 4 mm wire with 20 μm diameter would then have a resistance of 1.3 $\mu\Omega$. With three parallel wire bonds per connection and two connections in series in the circuit, this results in a total resistance of $2 \cdot R_{wb} = 0.87\ \mu\Omega$.

The resistance affects the signal in the SQUID in two ways. First of all, the resistance reduces the induced current in the pick-up loop circuit. Secondly, the resistance introduces Johnson noise over the signal.

The former can be calculated with an impedance transfer function approach. The voltage over the pick-up loop is the electromotive force from the flux change over time. In one cantilever oscillation, driven at the resonance frequency $f_{res} = 2700$ Hz:

$$|\mathcal{E}_{emf}| = \frac{\partial \Phi_L}{\partial t} = \frac{\Delta\Phi}{\Delta t} = \Delta\Phi \cdot f_{res} \tag{3.6}$$

The current induced in the circuit can be calculated by dividing the voltage amplitude by the total impedance.

$$|I(f = f_{res})| = \left| \frac{\mathcal{E}_{emf}}{2R_{wb} + i \cdot 2\pi f_{res} L_{tot}} \right| \tag{3.7}$$

where $L_{tot} = L_L + L_{tr} + 2 \cdot L_{wb} + L_{SQ}$ is again the sum of inductances in the circuit. This current is the same everywhere in the circuit, so also in the SQUID input coil, because all elements are in series. Assuming the same flux from the cantilever as calculated before, $\Delta\Phi = 20\ m\Phi_0$, the current amplitude is $I = 41.4\ pA$. The flux reaching the SQUID can then be calculated using the mutual inductance M_{in}

$$\Phi_{SQ} = M_{in} \cdot |I(f = f_{res})| \tag{3.8}$$

The final result is then $\Phi_{SQ} = 48.85\ \mu\Phi_0$. This is considerably lower than with an entirely superconducting circuit, however it is still more than a factor 100 above the flux noise floor of the SQUID.

Johnson noise can be modelled as a voltage source in series with the resistor. The root mean square voltage amplitude/bandwidth v_{rms} of the noise is then given by

$$v_{rms} = \sqrt{4k_b T \cdot 2R_{wb}} \cdot \sqrt{BW} \tag{3.9}$$

where BW is the bandwidth considered, which in a resonance peak measurement will be limited by the peak width around the resonance frequency. Analogous to Eq 3.7 and Eq 3.8 for the signal voltage, this voltage noise can be converted to the current by dividing by the total impedance at the resonance frequency and multiplied by the mutual inductance to get the flux noise into the SQUID.

$$\Phi_{noise}/\sqrt{BW} = \left| \frac{\sqrt{4k_b T \cdot 2R_{wb}}}{2R_{wb} + i \cdot 2\pi f_{res} L_{tot}} \right| \cdot M_{in} \tag{3.10}$$

The result is a flux noise from Johnson noise of $\Phi_{noise} = 6.05\ \mu\Phi_0/\sqrt{Hz}$. This is much larger than the internal flux noise floor of the SQUID, so the Johnson noise will be limiting.

Then, in order to get a signal-to-noise ratio larger than 1 in a 4K measurement, the resonance peak of the moving cantilever will have to be resolved in a bandwidth of less than 65 Hz. The typical Q-factor of a cantilever in high vacuum is around $\sim 1 \cdot 10^4$ [12]. At the resonance frequency of $\sim 3 \cdot 10^3$ Hz, the resonance peak width will be $BW_{res} = f_{res}/Q = 0.3$ Hz, which is much smaller than the maximum bandwidth of 65 Hz. In fact, the total wire bond resistance R_{wb} could be two orders of magnitude larger than the estimate made earlier and the maximum bandwidth will be still be 0.65 Hz.

It can be concluded that the easyMRFM, as assembled now with aluminium wire bonds, is limited by Johnson noise, but will have a signal-to-noise ratio larger than 1 in experiments at 4K temperatures.

A large breathing room for the noise floor is important, because the estimates made in the above analysis do not consider all factors. For example, the calculation for R_{wb} ignores edge effects, but these might be relevant at the mesoscopic micrometer scale at these low temperatures. If it is found in experiment that, despite the expectation, the signal-to-noise ratio is actually lower than 1, a resonance peak signal might still be obtained using statistical analysis on repeated measurements.

Note that the results above concerning finite resistances do not apply to experiments at milliKelvin, where the aluminium bonds are superconducting and only the flux signal results from section 3.2 apply.

3.5 Measuring thermal cantilever motion

Previous sections have focused on estimating the coupling and expected signal, however it would be useful to measure the coupling in the final easyMRFM setup. To do this, the cantilever should be driven to a known deflection. The resulting signal in the SQUID can be used to calibrate the coupling to cantilever amplitude. The piezo drive does not provide this absolute cantilever deflection amplitude, because the mechanical coupling is unknown. Instead, the thermal motion of the cantilever can be used to calibrate the coupling.

The deflection of the cantilever in thermal motion can be calculated using the equipartition theorem for the one vibrational mode.

$$\frac{1}{2}k_B T_{eff} = \frac{1}{2}kx_{rms}^2 \tag{3.11}$$

where k is the spring constant of the cantilever, x_rms is the root mean square deflection amplitude, and T_{eff} is the effective temperature of the cantilever, which might be higher than the dilution refrigerator when under 50 mK due to thermalisation issues and the influence of external vibrations.

Operating in 10 mK, the expected T_{eff} of the cantilever is around 20 mK. For the typical cantilevers in our group, k is between 50 en 150 $\mu N/m$. This means the thermal deflection can be expected to be at least dozens of picometers and at best $x_{rms} = 0.1 - 0.2\ nm$. This corresponds to a flux difference of $\Delta\Phi = 20\mu\Phi_0$ in the pick-up loop, which will be transformed to 0.32 $\mu\Phi_0$. Comparing again with the flux noise level of the SQUID at 0.3 $\mu\Phi_0/\sqrt{Hz}$, it can be concluded that the thermal motion will probably only barely be visible above the noise floor. With a bad cantilever, the thermal motion might not be measurable at all.

Chapter 4

Characterising cantilevers at room temperature

The central component of Magnetic Resonance Force Microscopy is a small flexible cantilever with a magnet attached to the end. The cantilevers are produced as chips, but in the Oosterkamp group we generally have the MRFM cantilever chips mounted in very inaccessible setups (for example: mounted in place in a dilution refrigerator). A room temperature setup where the cantilever can easily be swapped out was made by Tim Fuch, specifically to test the cantilever chips before mounting them in a more permanent setup. This accessible setup has the cantilever in high vacuum and it can be driven by a small piezo element mounted under the cantilever chip. The cantilever deflection is measured by aiming a laser beam on the cantilever tip with an optical fiber and taking the interference signal between the light reflecting back into the fiber from the cantilever and back reflection of the fiber end itself. See Fig 4.1a for a schematic overview of the optical setup. Additionally, a strong homogeneous magnetic field can be applied over the cantilever in the direction of the cantilever with an Helmholtz coil engulfing the vacuum chamber. This opens up options to characterise the magnetic properties of the cantilevers and experiment with their response to an external magnetic field. For example, knowing the resonance frequency beforehand is useful in identifying the resonance peak when the cantilever deflection signal-to-noise ratio is low and only a limited bandwidth is available.

4.1 Fringe visibility in the optical detection of cantilever deflection

The basis for the cantilever deflection detection is interference between the laser light back-reflected at the fiber end with intensity I_1 and the light reflecting back into the fiber from the cantilever with intensity I_2. The sensitivity of the optical setup is thus linked to the visibility ν of the interference fringes, which is defined as

$$\nu = \frac{2\sqrt{I_1 I_2}}{I_1 + I_2} \tag{4.1}$$

The first back-reflection inside the fiber can be modelled as a reflection on the flat surface between fiber material with breaking index $n_1 \approx 1.45$ and the vacuum with index $n_2 = 1$. With an incoming laser beam of intensity I_0, this reflection can be described as $I_1 = r_1^2 \cdot I_0$ with $r_1 = \frac{n_1 - n_2}{n_1 + n_2} = 0.184$. (or rather, the electric/magnetic field wave is reflected with a fraction r_1 and the intensity is the electric field magnitude squared).

The second beam is transmitted through this surface of the fiber as a fraction $t_1^2 = (1 - r_1)^2 = 0.816^2$ of I_0 and then diffracted as an Gaussian beam cone from the fiber. This beam of light hits the single-crystal silicon cantilever, $n_3 = 3.4745$, and is reflected back as a fraction $r_2^2 = 0.553^2$, which is then transmitted back into the fiber, again with a factor t_1^2. However, only a part of the beam cone hits the cantilever and then gets caught back into the fiber core, because the beam width has widened compared to the initial fiber beam waist due to diffraction. This can be accounted for with a factor η^2 that depends on geometry. The total expression for the visibility is then

$$\nu = \frac{2\eta r_1 t_1^2 r_2}{r_1^2 + \eta^2 t_1^4 r_2^2} \tag{4.2}$$

The main controllable variable is the distance d between the fiber and cantilever. The visibility is highest when the intensities match in Eq 4.1. This actually corresponds to a finite optimal distance, because with the cantilever too close to the fiber, too much light is captured back into the fiber and I_2 is much larger than I_1. To find the optimal distance, an expression for η needs to be derived.

The beam has an initial waist radius w_0 equal to the radius of the fiber core, 4.7 μm. The light then propagates in the x-direction as a Gaussian beam, because the typical wavelengths of the laser are much smaller than

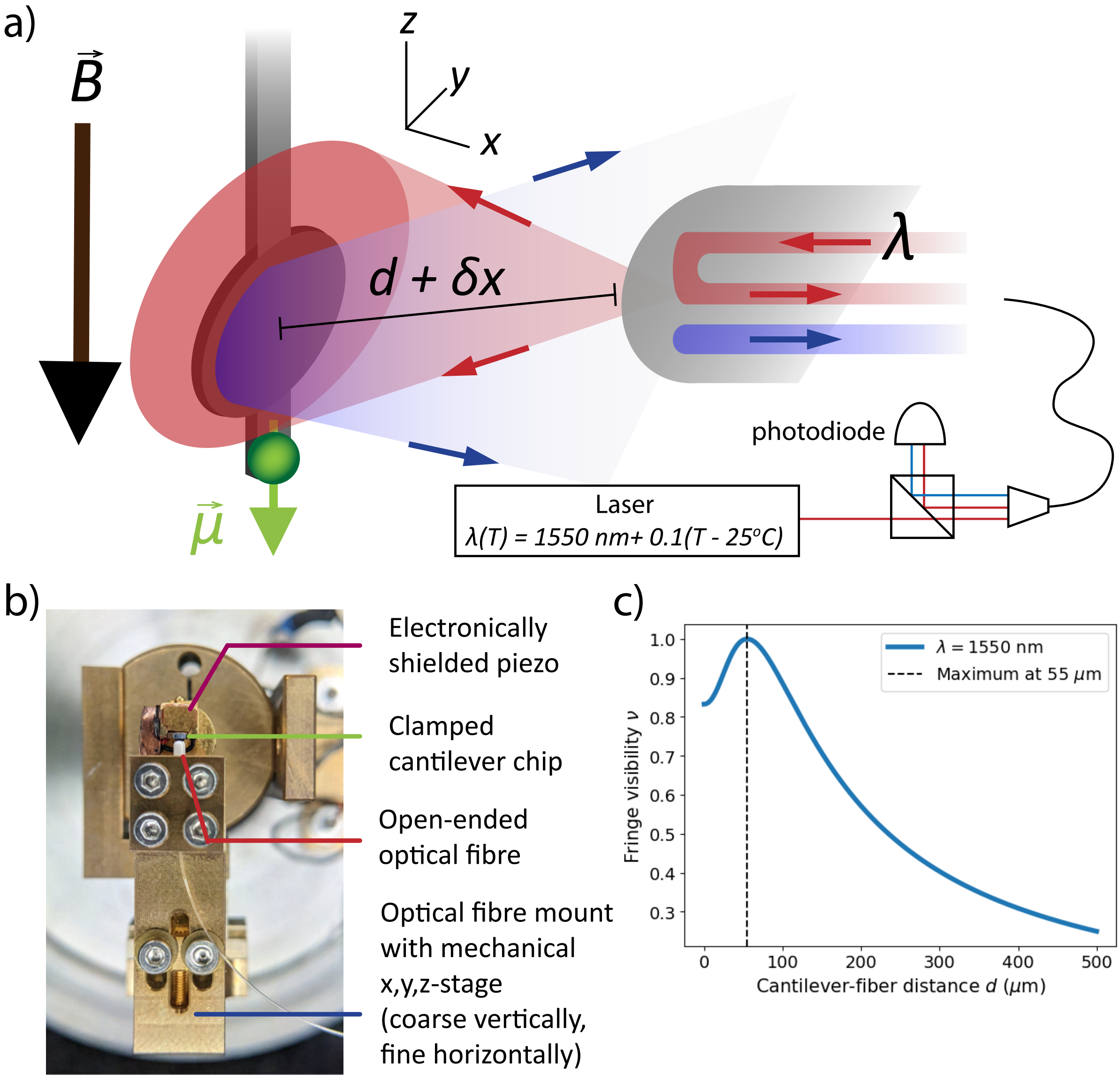

Figure 4.1: ***(a)*** *A schematic overview of the optical magnetometry setup to test cantilever chips in high vacuum at room temperature. A laser of wavelength* $\lambda = \lambda_0 + 0.1nm \cdot (T_{las} - 25C^\circ)$*, depending on separately-controlled laser temperature* T_{las} *and typical lambda*$_0 = 1550nm \pm 20$ *(not tested), is coupled to an optical fiber (red). Part of the light exits the fiber, while some light is back-reflected. The light exiting the fiber hits the cantilever and a fraction is reflected (blue) back into the fiber. The interference signal between the red and blue beam, depending on the fiber-cantilever distance, is a measure of the cantilever deflection* δx*. An homogeneous magnetic field* $\vec{B}$ *can be applied over the cantilever that interacts with the magnetic dipole* $\vec{\mu}$ *on the tip, analogous to Fig 1.1.* ***(b)*** *Picture of the vacuum probe with the setup. The ideal cantilever-fiber distance d is around 0.3 mm.* ***(c)*** *Visibility of the fringes in the interference signal, as function of d.*

the fiber core. The radius-dependent intensity of the Gaussian wave front widens proportionally with

$$I(r,x) \sim exp\left(\frac{r^2}{w(x)^2}\right) \tag{4.3}$$

$$w(x) = w_0\sqrt{1+(x/x_R)^2} \text{ with } x_R = \frac{\pi w_0^2 n_2}{\lambda} \tag{4.4}$$

where r is the radius in the y, z-plane and $w(x)$ is the growing beam waist.

With the light hitting a circular aperture, the fraction of the light outside of the aperture is lost. The cantilever, at a propagation distance $x = d$, has a large flat circular section with a radius of 7.5 μm that is intended to increase the amount of reflected light. The reflected light maintains the same Gaussian wave front and will continue to widen the waist while propagating back to the fiber, which can similarly be regarded as a circular aperture at $x = 2d$. The fiber aperture is both smaller than the cantilever aperture and $w(2d) > w(d)$. Therefore, even though some light is lost in the cantilever reflection, the fiber aperture is limiting and the reflection at the cantilever can be neglected as a factor in η. (The cantilever aperture does create some small diffraction effects along the edges of the beam, which are mostly irrelevant for the centre light that is hitting the fiber.)

The geometric factor η^2 can be defined as the fraction of the power carried by a Gaussian beam coming out of the fiber I_{out} to the power going back in I_{in}, if there were ideal reflection and transmission. Combining Eq 4.3 with the aperture radius of the fiber $r = w_0$, and $x = 2d$ gives

$$\eta^2 = \frac{I_{in}}{I_{out}} = 1 - exp\left(-\frac{2}{1+\left(\frac{2d\lambda}{\pi w_0^2}\right)^2}\right) \tag{4.5}$$

The beam is diverging, so all of the light hitting the fiber core will only be the light in the centre, with a smaller angle with the axis than the light at the edges of the Gaussian beam close to the diffraction angle of the fiber. Therefore, the numerical aperture does not limit the amount of light transmitting back into the fiber and thus does not factor into η and the visibility.

A factor that does come in play for the visibility, but that will not be considered here, is the spatial coherence. The visibility for any d will therefore in reality be a little lower then calculated, not reaching $\nu = 1$ at the peak.

The final expression for the visibility will then be a function of the variable cantilever-fiber distance d. Fig 4.1c visually illustrates the dependence of the fringe visibility on these variables. The maximum visibility for the setup can be achieved with $d = 55\ \mu m$. However, although the fine positioning stage in the y,z-plane allows for precise centering of fiber core under the cantilever reflective aperture under a microscope, the coarse approach stage of the fiber to the cantilever does not allow precision to 55 μm. To avoid breaking off the cantilever, a more safe distance of up to 400 μm should suffice, with a visibility of $\nu = 0.3$.

The typical wavelength of the laser should be 1550 nm at 25°C. However, the laser used in the setup has not been tested and, according to the manufacturer, could have a wavelength in the range 1530-1565 nm. The wavelength in the setup can be controlled as well by changing the temperature of the laser cavity, adding 0.1 nm per Kelvin.

The visibility also depends on the wavelength. However it turns out that neither the inherent range in the baseline wavelength, nor the controllable range changes the visibility more than 1% at any cantilever-fiber distance. This means that the dependence of the visibility on the wavelength should be negligible, especially concerning the controlled temperature.

The wavelength does effect the signal strength, though, because it affects the phase difference acquired between the immediately back-reflected light and the optical path reflecting against the cantilever. This phase difference depends on the path length difference, which is $2d + \delta x$, where δx is the cantilever vibration amplitude (ignoring spatial coherence considerations of a diverging Gaussian beam). The phase acquired along this path is $\phi = 2\pi(2d + \delta x)/\lambda$, resulting in an interference signal

$$I_{sig} \sim cos^2\left(\frac{2\pi \cdot 2d}{\lambda(T)} + \frac{2\pi\delta x}{\lambda(T)}\right) \tag{4.6}$$

The cantilever deflection is generally smaller than the wavelength, so the signal will oscillate within one fringe. With $d = 400\ \mu m$, a wavelength difference of 5 nm ($\Delta T = 50$°C) can shift the signal through more than 3 fringes.

4.2 Measuring the frequency shift in a homogeneous magnetic field

In terms of cantilever mechanics, the optical magnetometry setup can be modelled by a cantilever in an homogeneous magnetic field, which may not be perfectly aligned with the cantilever orientation. This model was discussed theoretically in section 1.2 of the introduction. With relation

Eq 1.10 it was concluded that the resonant frequency f_{res} of the cantilever shifts linearly with the magnetic field strength, for small deflections compared to the cantilever length.

$$f_{res} \approx f_0 + \frac{\pi}{m}|\mu| \cdot |B| \left(\frac{\alpha}{l}\right)^2 cos(\theta_0) \tag{4.7}$$

where f_0 is the cantilever resonance frequency without a field, $|B|$ is the external magnetic field strength, m is the mass of the cantilever, $|\mu|$ the magnetic dipole moment of the magnet on the cantilever tip, l the cantilever length, α the geometric factor compensating for the reduction of the effective cantilever length when bend during deflection, and θ_0 the misalignment angle of the magnetic field to the cantilever rest position in zero field.

As in the easyMRFM setup, the cantilever can be driven mechanically with a piezo element installed under the cantilever chip (see Fig 4.1b). The sinusoidal input voltage to vibrate the piezo can couple to the optical output of experiment through the cantilever deflection. The resonance response can then be measured for different constant $|B|$ by sweeping the input frequency of the piezo vibration while keeping the amplitude the same, resulting in a transfer function. A Zurich Instruments lock-in amplifier was used to monitor the periodic deflection signal from the photodiode at the frequency of the driving signal. The transfer function between this driving signal and the deflection signal can be fitted with a Lorentzian peak to determine the resonance frequency and Q-factor.

The magnetic field strength, generated by a Helmholz coil, can be controlled in the optical magnetometry setup by varying the DC current through the coil. The resonance frequencies for different field strengths were found for a set of available cantilever chips. The results can be found in Fig 4.2. Because a linear relation is expected and also observed, the results can be fitted by a linear function $f_{res} = f_0 = a \cdot |B|$ where the slope, as per Eq 4.7, should be given by $a = \frac{\pi}{m}|\mu| \cdot \left(\frac{\alpha}{l}\right)^2 cos(\theta_0)$. So the slope is determined by cantilever properties, combined with θ_0.

Having a method available to measure these cantilever properties is useful, because not all are easily controllable during fabrication. Both l and α are well-determined, because they depend on cantilever geometry on the scale of 10 μm, which is visible with optical microscopy. However, m and $|\mu|$ depend on the nano magnet at the tip. The method to select and attach the magnet is less consistent in magnet size, and in turn the final cantilever mass and magnet dipole moment. Although an estimate can be made (see section 2.1), it is the variation in the ratio $\frac{|\mu|}{m}$ that is responsible for the variation in the slope, even when cantilever geometry is the same as when comparing cantilevers T6 and T7 (Fig 4.2a and b.

A perfect determination of $\frac{|\mu|}{m}$ is impeded by the misalignment angle θ_0 of the external field. The coil and vacuum insert probe with the mounted cantilever chip (Fig 4.1b) are aligned by eye with no mechanism to adjust as the setup is operational. By visual estimate, the possible misalignment may be up to $\theta_0 = 10^\circ$, which would correspond to a 2% difference in the slope a, and thus $\frac{|\mu|}{m}$.

All four cantilevers could be dismounted without damage, to be used in other setups. This showcases that the optical setup is successful in its goal to test MRFM cantilevers to be used elsewhere.

4.3 Driving the cantilever magnetically

In the situation with a finite magnetic field, but without mechanical piezo drive, the cantilever will be deflected to a static equilibrium. The magnetic force F_B and restoring harmonic force F_k, as discussed in section1.2 of the introduction (Eq 1.8), balance out to zero. From there we can get an expression for the equilibrium deflection x_{eq}.

$$0 = F_B + F_k = -\left(k + |\mu| \cdot |B| \left(\frac{\alpha}{l}\right)^2 cos(\theta_0)\right) \cdot x + |\mu| \cdot |B| \frac{\alpha}{l} sin(\theta_0) \tag{4.8}$$

$$x_{eq} = \frac{|\mu| \cdot |B| \frac{\alpha}{l} sin(\theta_0)}{k + |\mu| \cdot |B| \left(\frac{\alpha}{l}\right)^2 cos(\theta_0)} = \frac{|\mu| \cdot |B| \frac{\alpha}{l} sin(\theta_0)}{f_0^2 m/4\pi^2 + |\mu| \cdot |B| \left(\frac{\alpha}{l}\right)^2 cos(\theta_0)} \tag{4.9}$$

where k is the stiffness of the cantilever, which can be substituted by a measured f_0 using $f_0 = 2\pi\sqrt{k/m}$. This expression makes sense in the limits for the magnetic field strength. For $|B| \to \infty$ we get $x_{eq} \to \frac{l}{\alpha} tan(\theta_0)$, which corresponds with the cantilever angle θ fully aligned with the angle of the magnetic field θ_0. With $|B| \to \infty$ the cantilever returns to its original equilibrium position $x_{eq} = 0$.

Interestingly, the expression in Eq 4.9 does not contain the mass m and dipole moment $|\mu|$ as a ratio like in the piezo drive experiment. Furthermore, the combination of unknowns $|\mu|$ and θ_0 do also not appear strictly co-linear with each other (eg $|\mu| sin(\theta_0)$ and $|\mu| cos(\theta_0)$). This provides an opportunity for an independent method to determine these three quantities.

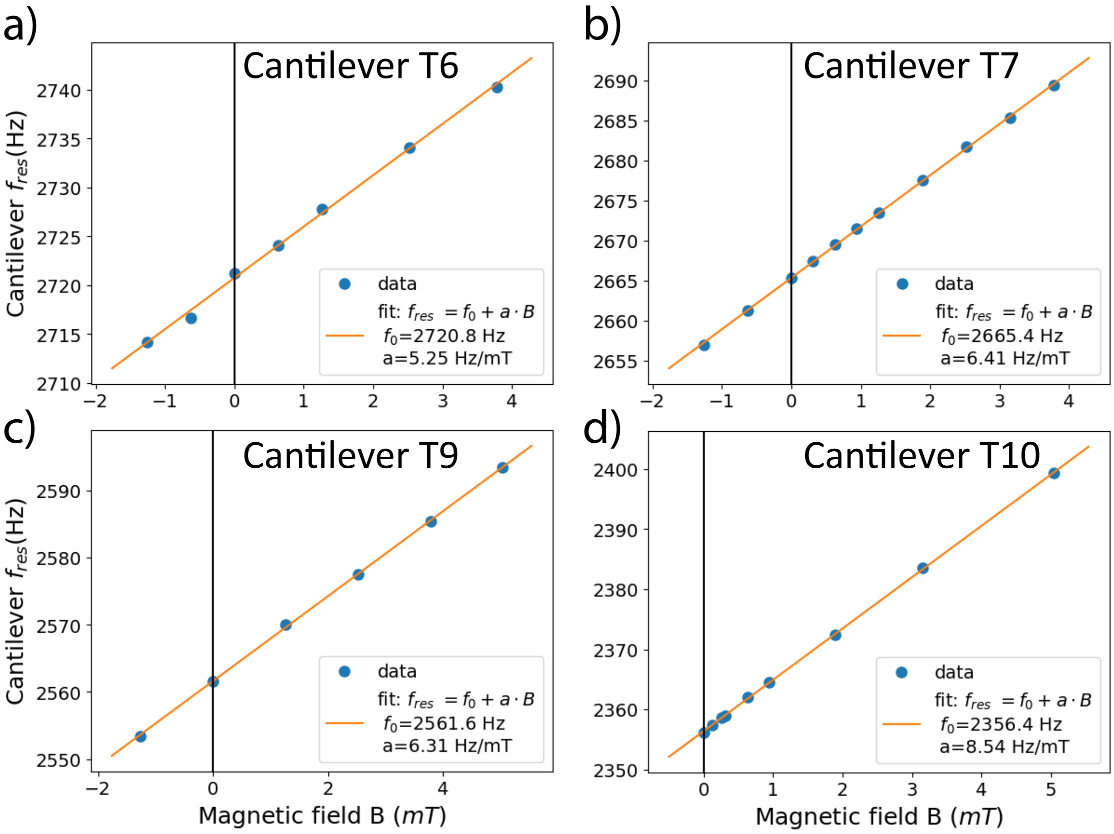

Figure 4.2: *Observation of the shift of the cantilever resonance frequency in the optical magnetometry setup. The frequency response of the cantilever deflection was measured by sweeping the driving frequency of a piezo mechanically coupled to the cantilever chip. This frequency response was then fitted with a Lorentzian peak to find the resonance frequency. Q-factors ranged from* $5 \cdot 10^3$ *to* $10 \cdot 10^3$*.* ***(a)-(d)*** *show the results different cantilever chips. Error bars, determined by the bandwidth of the resonance peak* ($= f_0/Q$)*, were less 0.5 Hz and therefore not drawn. The results were fitted with a linear function* $f_{res} = f_0 + a \cdot B$.

In an experiment, the magnetic field could be swept over a long range. If this $|B|$-sweep is performed over timescales much slower than the resonant frequency of the cantilever, the cantilever can be considered to be in the equilibrium deflection at all times. In a sense, the cantilever is driven magnetically. The deflection signal can be plotted against $|B|$ and fitted according to Eq 4.9, with f_0 and α/l as fixed values.

4.4 Detection of the thermal motion of the cantilever

With both the magnetic field and the piezo drive turned off, a peak in the interference signal was still observed at the resonance frequency of cantilever T7, while the phase was entirely incoherent. The measurement can be found in Fig 4.3.

This observation can be interpreted as the thermal motion of the cantilever. As discussed in chapter 3, the expected root mean square deflection amplitude can be derived from the equipartition theorem.

$$x_{rms} = \sqrt{\frac{k_b T}{k}} \tag{4.10}$$

with k and T the stiffness and the temperature of the cantilever. The optical magnetometry setup operates at room temperature With the typical stiffness of an IBM-cantilever of 100 $\mu N/m$ and $T = 300$, the thermal fluctuations would result in a deflection of $x_{rms} = 6.5\ nm$.

Since the amplitude of the thermal motion is well-defined, this measurement could be used to infer the relation between the absolute cantilever deflection distance and the photodiode current signal.

The measured peak in the signal in Fig 4.3 could also be attributed to other sources of incoherent noise. The effect of external vibration noise would look similar and could be responsible, although the experiment is setup on a negative-k plate and should have some vibration isolation. A broader analysis of the noise sources needs to be conducted before the measured signal can definitively be attributed to thermal fluctuations. For example, if external vibrations are responsible, there would be correlations between measured vibrations outside of the setup and the undriven cantilever motion.

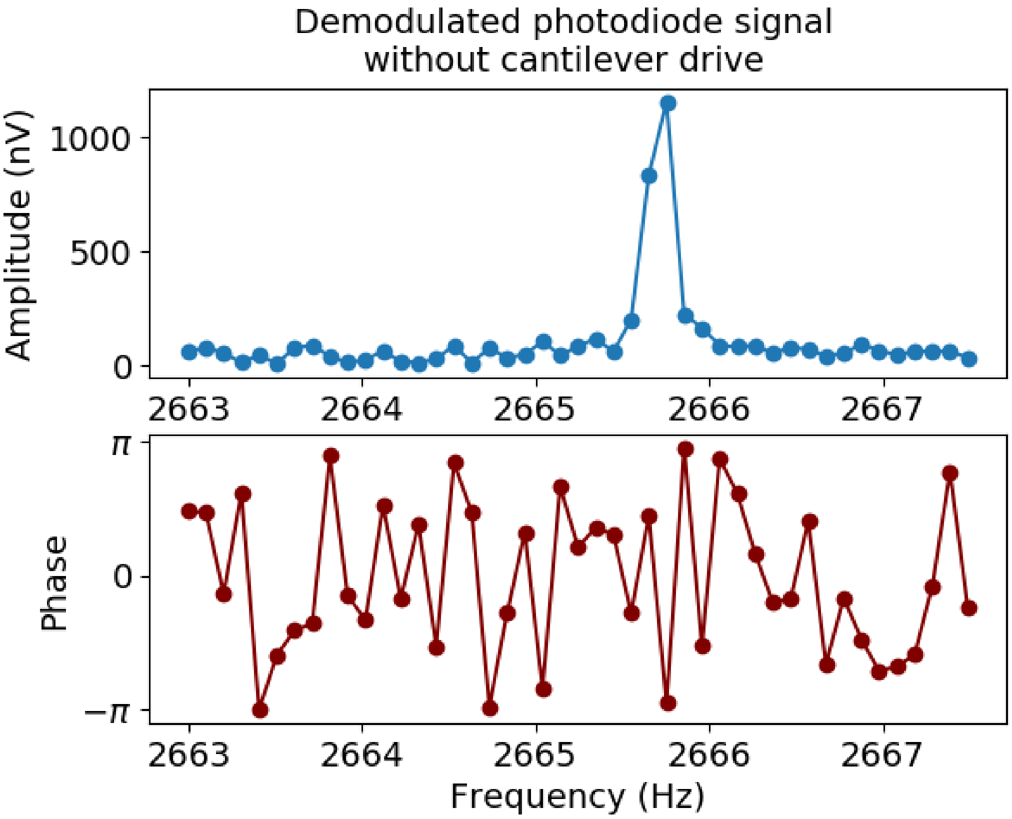

Figure 4.3: *Frequency sweep of the demodulated deflection deflection signal for the T7 cantilever when not driven. A peak in the amplitude can be observed at the resonance frequency, while the phase is incoherent across the spectrum. This peak can be attributed to thermal motion*

Chapter 5

Future steps towards magnetic resonance experiments

As it is currently assembled, the easyMRFM is a Magnetic Force detection device. However, there is of yet no possibility to do Magnetic Resonance experiments with the easyMRFM, because the polarising B_0-field and the spin-driving B_1 are still absent in the current device. Furthermore, some additional requirements need to be met to do the experiments on Al-Al_2O_3-Al Josephson junctions in qubits, as proposed in the introduction. The steps and technical requirements necessary for the easyMRFM in the future are discussed in this chapter.

5.1 B_0-field with Plugge coil

The main purpose of the magnetic B_0-field is to split the electron states using the Zeeman effect and magnetically polarise the electron population between these states according to Boltzmann statistics. With a larger polarisation, more electrons participate in an electron resonance experiment. The strength of the field does not necessarily need to be very strong in SQUID-detected MRFM, because the method is very sensitive and only a small population electrons needs to be polarised to produce a measurable signal above the force noise limit.

In the application to superconducting Al-Al_2O_3-Al Josephson junctions, however, the B_0-field needs to serve an additional purpose that will set the lower bound to the required magnetic field strength in the easyMRFM. Due to the Meissner effect, all magnetic fields will be shunned from the interior of the sample by the superconducting aluminium on the ex-

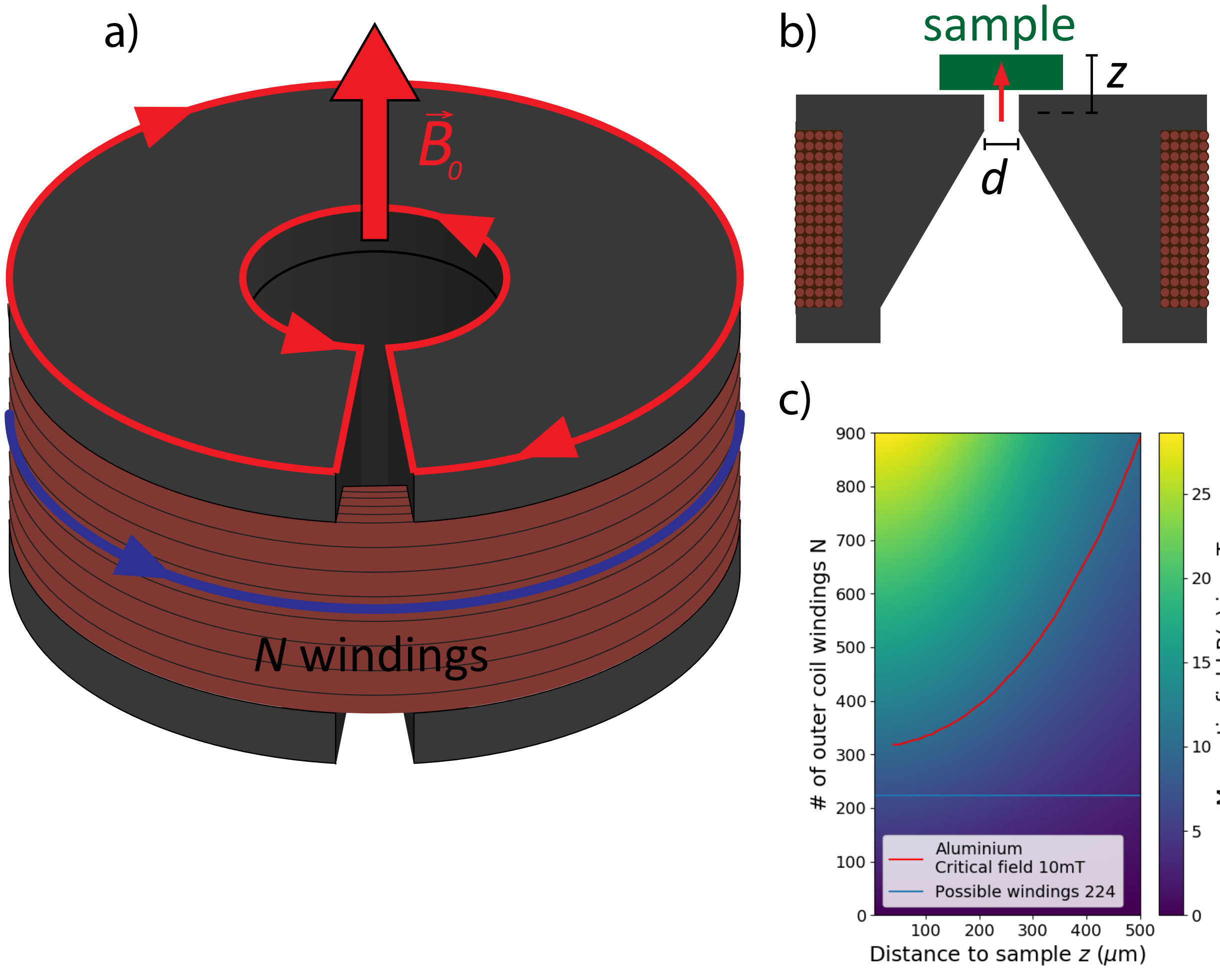

Figure 5.1: **(a)** *Schematic of the Plugge coil design[19]. A current (blue) is induced in a NbTi wire coil (brown) wound around a superconducting core (grey). Due to the Meissner effect, the magnetic field produced by this outer coil is expelled from the core with surface currents (red). These surface currents are forced to run through an inner loop because of groove to the centre hole in the core. This inner loop generates the* B_0*-field.* **(b)** *vertical cross section of Plugge coil, with sample placement in green. labelled are the centre loop diameter d and distance between loop and upper surface of the sample z.* **(c)** *Calculated maximal magnetic field strength* $B_0(z, N)$ *as function of z and number of windings N in the outer coil. The maximal current in the outer coil* $I_outer \approx 0.032\ A$ *was used, which is limited due to Joule heating. The critical field of Aluminium (10 mT) is shown in red. The line* $N = 224$ *indicates the largest amount of windings possible with the materials at hand.*

Version of August 30, 2021– Created August 30, 2021 - 14:44

terior. This both prevents the polarisation of the electron population and the read-out with the magnetic cantilever. The critical field strength of aluminium is 9.9 mT [20][16] at 10 mK (10 mT at absolute zero) and this is therefore the required minimum in order to perform electron resonance experiments on these Josephson junction qubit devices.

A local magnetic field that is only present in the sample is the preferred option for the B_0-field in the easyMRFM. As discussed in section 1.2 of the introduction and in chapter 4, an homogeneous magnetic field affects the cantilever dynamics. More importantly, a strong enough field to break superconductivity in the sample, will also break it in the aluminium wire bonds between the pick-up loop chip and the SQUID chip when this field is homogeneous over the whole setup. This would introduce Johnson noise in the flux that will overshadow the MRFM signal (see section 3.4 in chapter 3). Exceeding the critical field will not so soon be a problem for niobium (or NbTi) connections, with critical fields as high as 0.82 T (or 15 T)[16]. Furthermore, none of the available dilution refrigerators in the lab have the setup for a large coil to produce large external fields, nor is it practical in dipstick experiments. A local coil build into the easyMRFM offers the most flexibility in use.

The sample mounting arm of the simple easyMRFM sample stage can be swapped out for a version on which a magnetic coil can be mounted, with the B_0-field pointing in the z-direction. The sample can then be glued on top of the coil to get the sample in close proximity to the point at which the field is strongest. As with the simple sample stage arm, the coil-sample version can approach the cantilever, with the sample on the cantilever side.

The coil design of choice is the Plugge coil, a device recently developed in our lab[19]. A schematic of a Plugge coil can be found in Fig 5.1a, with a cross section in b. The Plugge coil consists of a superconducting core with a coil wound around. The core has a small hole through the middle (diameter $d = 0.5\ mm$) which is connected to the outside with a sideways groove. In essence, it functions as a transformer of a current in the wound coil on the outside to the inner loop via the Meissner effect. The field of the outer coil is expelled from the core with a current that primarily runs over the surface of the superconductor in tangential direction. The groove forces this surface current to run through the centre loop as well, which produces a very local field that is used as B_0.

The current through the centre loop I_{inner} can be calculated for any the outer coil current I_{outer} using the expression for a transformer.

$$\frac{I_{inner}}{I_{outer}} = \frac{N_{outer}}{N_{inner}} \cdot \kappa \tag{5.1}$$

where N_{outer} and N_{inner} are the number of windings and k is the unit-less efficiency of the transformer. Experiments with Plugge coils have shown that κ is at least 0.8.

The centre hole can be approximated as a single loop, $N_{inner} = 1$. The number of windings on the outer coil is limited by the geometry of the core and the diameter of the used wire. The core has space carved out for the wire to be wound, which is visible in the cross section in Fig 5.1b. It is undesirable to have wired wound outside of this region because the wires will be spaced less consistently and the coil might produce a slight gradient field. In previously produced Plugge coil cores, the rectangular space is 4.16 mm x 1.0 mm. To avoid losses and heating of the sample, a superconducting wire should be used. Available in the lab is superconduting NbTi-wire with a diameter of 127 μm. The combination of this wire with the geometry allows for 32 windings next to each other and 7 stacks, adding to a total of $N = 224$ maximal windings possible with the materials available at the moment.

The limiting factor for the magnetic field strength comes from Joule heating in wires connecting to the wound outer coil. Even though this set of wires will be superconducting in the dilution refrigerator, they are heated at the regions outside the dilution refrigerator leading to the current source and conduct the heat well. A dilution refrigerator has limited cooling power to keep a setup at milliKelvin. In our lab this cooling power has been found to be around 1 μW and connecting wires into the cooled chamber were found to have resistances of around $\sim$ 1 $m\Omega$. Using the expression for Joule heating $P_{heat} = I^2 R$, the maximum current in the coil will be around $I_{outer} \approx 0.032$ A.

The maximum strength of the generated B_0-field can then approximated as that of the single centre loop with diameter d. The sample is positioned right on top of the centre loop and has a finite thickness. The relevant field strength would be at the far surface at a distance z from the middle of the loop (see Fig 5.1b). The field strength on the centre axis of an ideal loop is given by

$$B_0(z) = \frac{\mu_0}{4\pi} \frac{2\pi d^2 I_{inner}}{z^2 + d^2} \tag{5.2}$$

The colour map in Fig 5.1c shows the resulting field strengths in the sample at a range of distances z, using different numbers of outer coil windings, with the maximum allowed current applied on the Plugge coil.

An reasonably expected value for z in the case of the Al-Al_2O_3-Al qubit, mostly due to the thickness of the sample, will be around 300 μm. Even still, the B_0-field that can be generated using the components at hand (blue line) is less than the required 10 mT (red line) at $z = 0$. It is thus clear from this calculation that more work needs to be done before the application of the easyMRFM to investigate the qubit device.

The straightforward, but labour-intensive option would be to fabricate a new Plugge coil core that can accommodate more windings. However, more than twice the windings will be needed to reach 10 mT, and probably more windings to operate at a current that is not on the brink of heating the setup. This makes the Plugge coil more bulky, reaching dimensions that have not yet been experimented with.

Another option would be to use a transformer to amplify the limited current coming from warm wires to fully-superconducting wires, thermally-isolated from the warm wires, before connecting to the outer coil. This is the most practical solution, because transformers are more common part or even easy to fabricate ourselves. There is no inherent need to get a specific inductance, so the transformer can be somewhat sloppy.

A final issue concerning the B_0-field is its stability over time. The current source that is ultimately generating the field is not free of noise. The 1/f-noise and Johnson noise in the room temperature electronics might result in fluctuations of the B_0-field larger than the magnetic field sensitivity of the cantilever. This source of noise can be avoided by decoupling the electronics from the Plugge coil entirely with a persistent current switch, where a shortcut is made in a superconducting circuit with the coil right as the circuit connection to the current source is cut off. The supercurrent already present in the Plugge coil can persist up to years at a very stable current value and continue generating the B_0-field.

A persistent current switch may not be a necessity for the easyMRFM, but it might aid in its range of samples by accommodating to more spin sparse samples that still need a strong magnetic field. If a persistent current switch is used and electronics are added on the cold side of the dilution refrigerator setup anyway, it would be the natural choice to use the transformer option to increase the maximum allowed current in the coil.

5.2 Options for the B_1-field

In previous SQUID-detected MRFM setups the B_1-field was generated by a current through a straight rf wire that was lithographically printed close the similarly printed pick-up loop. This method has all the same disadvantages as with the printed loop and the B_1-field should be integrated as part of the probe head as well.

Three options can be considered. The first would be to attach an electromagnet to the probe head. This can readily be integrated by gluing a simple superconducting wire loop to the copper mounting structure next to the cantilever chip mount. The wire loop can be carefully moulded to be positioned close to the cantilever tip. Although, even if the loop can be positioned as close as possible, the generated field might not be sufficient for MRFM. Alternatively, a transformer could be used to increase the field strength and allow for larger fields and a safe distance from the cantilever.

The second and third option make use of the higher order modes of the magnetic cantilever to generate the B_1-field. The cantilever can simultaneously be driven at the first mode to monitor the frequency shift and driven in higher modes to create a changing magnetic field with a vibrating magnetic tip at these higher mode frequencies. These well-defined frequencies cover a select few very thin resonant slices under the sample surface by virtue of the high Q-factor of the cantilever. This B_1 scheme has been accomplished in SQUID-detected MRFM before [11]. Other advantages include the guaranteed proximity of the generated field to the location of measurement on the sample and the strong field strength changes due to the large field gradient of the cantilever tip nanomagnet.

The piezo element that is already installed in the easyMRFM to drive the cantilever in the first vibration mode, can be used to drive to higher modes as well. Using this method, no further hardware would need to be added to the device to produce a B_1-field. Although it is questionable whether the higher cantilever modes can be driven to large enough amplitudes with the piezo, because more energy is required for similar amplitudes with increasing modes.

Instead, the cantilever could be driven by a magnetic field which, similarly to option one, would be produced by a simple wire loop installed next to the cantilever. This loop field would probably not need to be amplified with a transformer, because the cantilever modes will effectively amplify the field.

Either of these three option could be pursued to generate the B_1-field. For a first proof of concept of the easyMRFM performing complete MRFM, the piezo drive option would be a good start, because it does not require any additional assembly.

Chapter 6

Conclusions

The most critical fabrication challenges of the easyMRFM have been overcome, with the cantilever, pick-up loop, and SQUID chip mounted on the single probe head.

The positioning stage for the pick-up loop chip has been demonstrated to reliably enable the relative cantilever-loop positioning that should theoretically result in a MRFM setup that can detect the thermal cantilever motion at milliKelvin. With a model for the coupling strength, the signal strength of the thermal motion in the SQUID has been calculated to be 0.32 $\mu\Phi_0$ with a minimal bandwidth of $\sim$ 0.3 Hz, against the flux noise in the SQUID of 0.3 $\mu\Phi_0/\sqrt{Hz}$. Although this is not a large margin of error, the function of the detection of the thermal motion is mainly necessary to calibrate the system. In the driven cantilever mode of operation, the signal strength might be up to three orders of magnitude larger, with the noise unchanged.

Furthermore, it has been demonstrated that, theoretically, the coupling should also be strong enough to observe a signal from a driven cantilever in a liquid helium dipstick experiment. During assembly there had to be resorted to aluminium wire bonds, which are not superconducting at 4 K, instead of niobium wire bonds. It was found that the the main relevant consequence of this design choice is the introduction of Johnson noise to the pick-up loop circuit. The expected driven maximum signal amplitude in dipstick experiments is 48.85 $\mu\Phi_0$, against the flux noise due to Johnson noise of 6.05 $\mu\Phi_0/\sqrt{Hz}$. This allows for the positioning optimising process to be carried out in dipstick experiments.

The clear next step will be to do a dipstick experiment and detect the driven cantilever signal. This can then be repeated with a range of cantilever-loop positions, so the coupling can be optimised. Unfortunately, after one dipstick experiment with a snap-to-contact from the cantilever to the loop chip and hence no signal, the soldering to the SQUID chip broke. In an attempt to fix this, both the cantilever and loop chip were destroyed. This means the assembly process will need to be repeated in the near future.

After that, the coils for the B_0 and B_1 fields will need to be installed. Their assembly is less challenging, because only a few fabrication steps at micron scale are required. The developed MRFM probe head will be completed and ready to investigate previously inaccessible samples at milliKelvin temperatures. The easyMRFM will transition, in a sense, to a plug-and-play device.

Chapter 7

Acknowledgements

I would like to thank everyone in the Oosterkamp Group for having me around for the last 7 months. A special thanks to Tim Fuchs, who supervised me. He did everything in his power to not only make progress with the project, but to teach me loads of skills along the way. Now I know how to operate a turbo pump and how to hold tweezers steady.

I would also like to thank Jaimy Plugge. As the only other PhD student around, you were able to help me whenever Tim could not. Your efforts to wire bond niobium were also much appreciated. Maybe you'll succeed with niobium one day...

And lastly, I want to thank my fellow master students, Dennis Uitenbroek and Koen van Deelen. It was great that we could help each other out. I had a lot of fun, so thanks.

Bibliography

[1] V. V. Kruglyak, S. O. Demokritov, and D. Grundler, *Magnonics,* Journal of Physics D: Applied Physics **43** (2010).

[2] J. Kondo, *Resistance Minimum in Dilute Magnetic Alloys,* Progress of Theoretical Physics **32**, 37 (1964).

[3] J. R. B. John E. Wertz, *Electron Spin Resonance: Elementary Theory and Practical Applications*, Chapman and Hall, 1986.

[4] R. Wiesendanger, *Spin mapping at the nanoscale and atomic scale,* Reviews of Modern Physics **81**, 1495 (2009).

[5] S. Baumann, W. Paul, T. Choi, C. P. Lutz, A. Ardavan, and A. J. Heinrich, *Electron paramagnetic resonance of individual atoms on a surface*, Science **350**, 417 (2015).

[6] F. Casola, T. V. D. Sar, and A. Yacoby, *Probing condensed matter physics*, Nature reviews Materials **3**, 8 (2018).

[7] J. A. Sidles, *Noninductive detection of single-proton magnetic resonance*, Applied Physics Letters **58**, 2854 (1991).

[8] J. A. Sidles, J. L. Garbini, K. J. Bruland, D. Rugar, O. Züger, S. Hoen, and C. S. Yannoni, *Magnetic resonance force microscopy,* Rev. Mod. Phys. **67**, 249 (1995).

[9] D. Sarid, *Scanning Force Microscopy: With Applications to Electric, Magnetic, and Atomic Forces (Oxford Series in Optical and Imaging Sciences)*, US Patent 5,319,960 (1994).

[10] C. L. Degen, M. Poggio, H. J. Mamin, C. T. Rettner, and D. Rugar, *Nanoscale magnetic resonance imaging,* Proceedings of the National Academy of Sciences of the United States of America **106**, 1313 (2009).

[11] M. De Wit, G. Welker, J. M. De Voogd, and T. H. Oosterkamp, *Density and T1 of Surface and Bulk Spins in Diamond in High Magnetic Field Gradients*, Physical Review Applied **10**, 1 (2018).

[12] M. De Wit, G. Welker, J. J. Wagenaar, F. G. Hoekstra, and T. H. Oosterkamp, *Feasibility of imaging in nuclear magnetic resonance force microscopy using Boltzmann polarization*, Journal of Applied Physics **125** (2019).

[13] B. Chui, Y. Hishinuma, R. Budakian, H. Mamin, T. Kenny, and D. Rugar, *Mass-loaded cantilevers with suppressed higher-order modes for magnetic resonance force microscopy,* in *TRANSDUCERS '03. 12th International Conference on Solid-State Sensors, Actuators and Microsystems. Digest of Technical Papers (Cat. No.03TH8664)*, volume 2, pages 1120–1123 vol.2, IEEE, 2003.

[14] S. J. Bosman, *Delft Circuits b.v.*, 2021.

[15] D. J. Thoen, B. G. C. Bos, E. A. F. Haalebos, T. M. Klapwijk, J. J. A. Baselmans, and A. Endo, *Superconducting NbTiN Thin Films with Highly Uniform Properties over a 100 mm Wafer*, page 1 (2016).

[16] B. T. Matthias, T. H. Geballe, and V. B. Compton, *Superconductivity*, Rev. Mod. Phys. **35**, 1 (1963).

[17] W. Jaszczuk, H. J. Ter Brake, J. Flokstra, D. Veldhuis, R. Stammis, and H. Rogalla, *Bonding of a niobium wire to a niobium thin film,* Measurement Science and Technology **2**, 1121 (1991).

[18] J. H. Ribot, J. Bass, H. Van Kempen, R. J. Van Vucht, and P. Wyder, *Electrical resistivity of aluminum below 4.2 K*, Physical Review B **23**, 532 (1981).

[19] J. Plugge, *Generating High B0-Fields for use in Extremely Low Temperature MRFM,* (2020).

[20] J. F. Cochran and D. E. Mapother, *Superconducting Transition in Aluminum*, Physical Review **111**, 132 (1958).